DESIGN AND MODELING OF TURBINE AIRFOILS WITH ACTIVE FLOW CONTROL IN REALISTIC ENGINE CONDITIONS

Jeffrey P. Bons
Department of Mechanical Engineering
Brigham Young University, Provo, Utah

Abstract
Flow separation limits the efficiency of low-pressure turbines (LPTs) in aircraft engines. Experiments with vortex generator jets (VGJs), conducted in AFRL's low-speed cascade at Wright-Patterson AFB, have demonstrated dramatic reductions in separation losses. Before flow control can become an integral part of LPT design, research must be conducted in more realistic engine conditions. This can best be accomplished through a combined experimental and computational program that uses both tools in a complementary fashion. Such a program was initiated at BYU in 2007 to better understand the basic physics of the separation control phenomenon and establish the quantitative links between the underlying flow physics and LPT performance under a variety of conditions. A new, high performance LPT blade design (L1A) was received from AFRL. CFD was used to design a new 3-passage cascade facility with the L1A blade. The new cascade was completed at Ohio State University under a subcontract agreement between BYU and OSU since the PI moved to OSU in July 2007. CFD was also used to determine the appropriate diameter and location for an upstream wake generator. The wake generator was used to assess the impact of upstream wakes on the implementation of pulsed VGJ flow control for the Pack B baseline LPT design. The convecting wakes have a first order influence on the LPT flowfield.

Full Report
This report includes a summary of the three interrelated activities outlined above:
1. A preliminary evaluation of an upstream wake generator using CFD.
2. The comparison of VGJ experimental data with results from an LES solver.
3. The first series of results from the new L1A cascade facility.

Figure and reference numbering is independent for each section. The 2nd and 3rd topics were addressed in conference presentations and a more complete account can be found in paper #AIAA 2008-0558 presented at the AIAA 46th Aerospace Sciences Meeting and Exhibit in Reno, NV, 7-10 Jan 2008 and paper #GT2008-50864 presented at the 2008 IGTI conference in Berlin, 9-13 June 2008.

1

REPORT DOCUMENTATION PAGE

Public reporting burden for this collection of information is estimated to average 1 hour per response, including the time for reviewing instructions, searching existing data sources, gathering and maintaining the data needed, and completing and reviewing this collection of information. Send comments regarding this burden estimate or any other aspect of this collection of information, including suggestions for reducing this burden to Department of Defense, Washington Headquarters Services, Directorate for Information Operations and Reports (0704-0188), 1215 Jefferson Davis Highway, Suite 1204, Arlington, VA 22202-4302. Respondents should be aware that notwithstanding any other provision of law, no person shall be subject to any penalty for failing to comply with a collection of information if it does not display a currently valid OMB control number. **PLEASE DO NOT RETURN YOUR FORM TO THE ABOVE ADDRESS.**

1. REPORT DATE (DD-MM-YYYY)	2. REPORT TYPE	3. DATES COVERED (From - To)
16-07-2008	Final Report	From 1-1-07 to 31-12-07

4. TITLE AND SUBTITLE	5a. CONTRACT NUMBER
DESIGN AND MODELING OF TURBINE AIRFOILS WITH ACTIVE FLOW CONTROL IN REALISTIC ENGINE CONDITIONS	
	5b. GRANT NUMBER
	FA9550-07-1-0186
	5c. PROGRAM ELEMENT NUMBER

6. AUTHOR(S)	5d. PROJECT NUMBER
Jeffrey P. Bons	
	5e. TASK NUMBER
	5f. WORK UNIT NUMBER

7. PERFORMING ORGANIZATION NAME(S) AND ADDRESS(ES)	8. PERFORMING ORGANIZATION REPORT NUMBER
Brigham Young University Department of Mechanical Engineering 435 Crabtree Building Provo, UT 84602	

9. SPONSORING / MONITORING AGENCY NAME(S) AND ADDRESS(ES)	10. SPONSOR/MONITOR'S ACRONYM(S)
Air Force Office of Scientific Research 875 N. Randolph, Ste. 325 Rm. 3112 Arlington, VA 22203	AFOSR/NA
	11. SPONSOR/MONITOR'S REPORT NUMBER(S)
	AFRL-SR-AR-TR-08-0496

12. DISTRIBUTION / AVAILABILITY STATEMENT

Distribution A; distribution unlimited

13. SUPPLEMENTARY NOTES
NONE

14. ABSTRACT

Flow separation limits the efficiency of low-pressure turbines (LPTs) in aircraft engines. Experiments with vortex generator jets (VGJs), conducted in AFRL's low-speed cascade at Wright-Patterson AFB, have demonstrated dramatic reductions in separation losses. Before flow control can become an integral part of LPT design, research must be conducted in more realistic engine conditions. This can best be accomplished through a combined experimental and computational program that uses both tools in a complementary fashion. Such a program was initiated at BYU in 2007 to better understand the basic physics of the separation control phenomenon and establish the quantitative links between the underlying flow physics and LPT performance under a variety of conditions. A new, high performance LPT blade design (L1A) was received from AFRL. CFD was used to design a new 3-passage cascade facility with the L1A blade. The new cascade was completed at Ohio State University under a subcontract agreement between BYU and OSU since the PI moved to OSU in July 2007. CFD was also used to determine the appropriate diameter and location for an upstream wake generator. The wake generator was used to assess the impact of upstream wakes on the implementation of pulsed VGJ flow control for the Pack B baseline LPT design. The convecting wakes have a first order influence on the LPT flowfield.

15. SUBJECT TERMS
NONE

16. SECURITY CLASSIFICATION OF: UNCLASSIFIED			17. LIMITATION OF ABSTRACT	18. NUMBER OF PAGES	19a. NAME OF RESPONSIBLE PERSON Jeffrey Bons
a. REPORT UNCLASSIFIED	b. ABSTRACT UNCLASSIFIED	c. THIS PAGE UNCLASSIFIED	NONE	28	19b. TELEPHONE NUMBER (include area code) (614) 247-8414

Wake Generator Evaluation

Procedure

The purpose of this evaluation was to determine the appropriateness of cylinder wake generators to simulate the velocity deficit and turbulence parameters in the wake of a passing blade. An additional objective was to determine the proper cylinder diameter and upstream location for the BYU/OSU experimental setup.

The wind tunnel that will be used for experimentation is shown in Figure 1. It is a three passage cascade with a row of wake generating cylinders that move parallel to the inlet plane of the cascade, the cylinders moving at Uc=Uaxial/.85. The goal was to get the velocity characteristics at a plane parallel to the cascade inlet. The domain chosen for the numerical cylinder runs is shown above in Figure 1. This domain was chosen to follow the direction of the wake, vector sum of the axial and cylinder velocities, from the cylinder for ease of creating a grid. The stator blade was modeled as the L1M rotor blade rotated 10 degrees to get the flow angle to match the inlet flow angle of the L1A blade. The spacing between trailing edge of the stator cascade and the leading edge of the rotor cascade was taken to be 30% axial chord of the rotor. The data from this plane, mean flow and turbulence quantities, will then be matched with the data from the cylinder wake to find the distance downstream of the cylinder the rotors should be placed.

The Reynolds number of the upstream blade, Re=24000, was taken slightly higher than the Reynolds number of the rotor cascade, Re=20000. This was done to simulate the real effect of a stator on the flow, and make the rotor cascade comparable to previous experiments that were done with Re=20000. The solver used for the solution was the commercially available 2D Fluent Reynolds Averaged Navier Stokes using the RSM turbulence model. The flow over the blade was considered fully turbulent to avoid any separation because the desired wake was that of an attached flow. Due to wanting an attached flow, it was also necessary to keep the same solidity as the rotor cascade instead of using the solidity of a typical stator cascade.
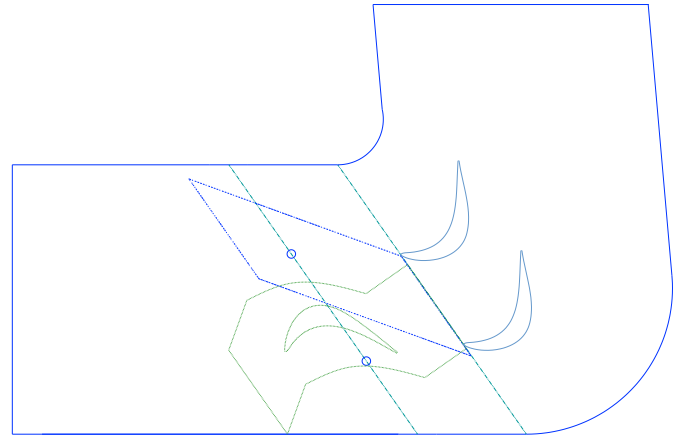

Figure 1. Sketch of the experimental tunnel geometry, including cylindrical wake generators. Also shown are the computational domains for the cylinder simulations and representative upstream blade simulations.

The axial velocity for the cylinder case was taken to be the same as the rotor blade. This made the cylinder Reynolds number in the range 1200 to 1500 depending on the diameter of the cylinder. This was done assuming the small cylinders would have minimal effect on the mean flow. This range of Reynolds numbers for cylinders make using a simple 2d model less meaningful. The solver used for the cylinder cases was SFELES, a quasi 3D large eddy simulation that would take into account the 3d aspects of the flow. This is appropriate because the upstream flow in the tunnel is essentially laminar and at the Reynolds number seen, the boundary layer on the cylinder is laminar, separation is laminar, and transition to turbulence occurs in the wake.

Results

Blade Wake

The computational domain consisted of a single blade with periodic conditions imposed at approximately the mid-passage, as seen in Figure 2. Near the blade, a structured quad mesh was generated to capture the boundary layer, shown in Figure 3. This boundary mesh had a spacing of $h_o/c=.001$ for the first point off the wall, and extended approximately $h/c=.00516$ from the wall.

Outside the boundary mesh, unstructured triangles were used to mesh the remainder of the domain. Approximately 125 points were used along the upper and lower blade surfaces. In total, approximately 40,000 cells were used in the mesh. A second, finer mesh containing 80,000 cells was used to indicate grid convergence based on the Cp distribution on the suction surface. The finer mesh was used for all solutions.
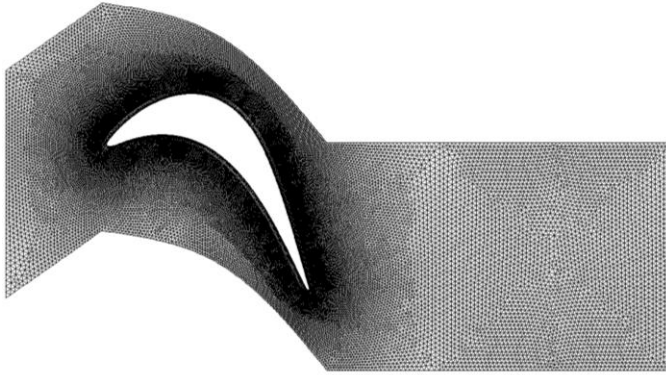

Figure 2. View of computational domain and mesh used for RANS simulations of the blade wake.
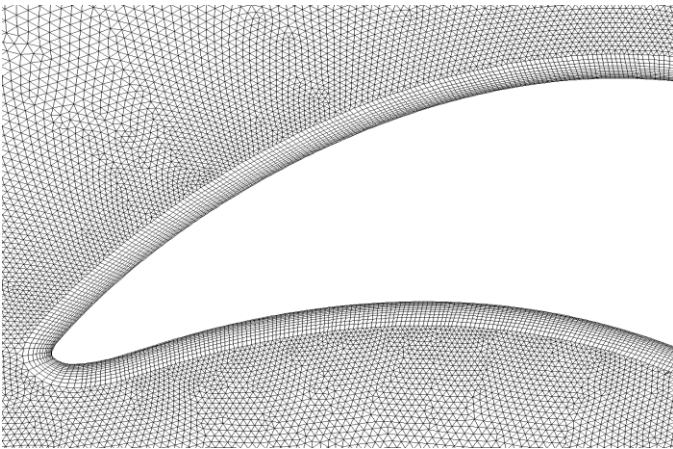
Figure 3. Close-up view of the mesh near the blade showing the boundary layer mesh near the wall.

The solution of the flow field can be seen in Figures 4 -8. Figure 5 shows the contours of velocity magnitude. It can be seen in this figure that the flow velocity increases over the top of the blade until it reaches a maximum value around 60% axial chord. This point also coincides with maximum Cp and static pressure as can be seen in Figure 4. After this point the boundary layer grows due to an adverse pressure gradient and viscous effects. The boundary

layer does not separate due to the turbulent effects of the flow. The low momentum flow created by the boundary layer extends past the trailing edge of the blade. This deficit in momentum will be examined and compared with momentum deficit created by the cylinder. It is important to note that the turbulence intensity grows inside the boundary layer where the viscous forces induce the creation of eddies. This increase in turbulence extends with the low momentum flow into the wake region, seen in Figure 6. The flow field was also solved with the k-ε turbulence model to validate general trends and compare turbulence values. The results were similar for the velocity deficit, but it can be seen that the k-ε model over predicts the turbulence intensity, see Figure 7 & 8.
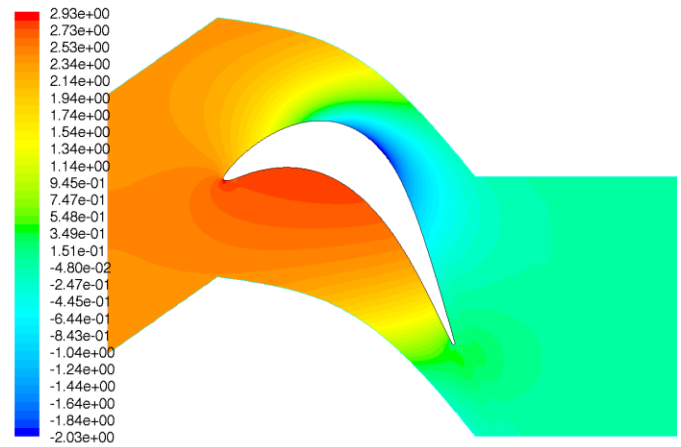

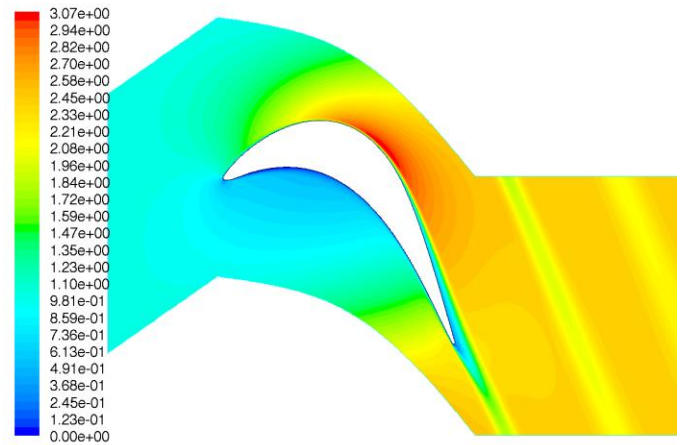**Figure 4. Contours of pressure for the simulation of flow past a periodic blade using the RSM turbulence model.**

Figure 5. Contours of velocity magnitude for the simulation of flow past a periodic blade using the RSM turbulence model.
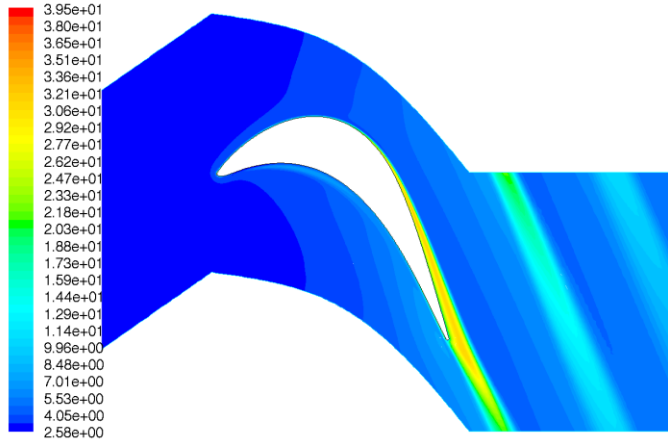
Figure 6. Contours of turbulence intensity for the simulation of flow past a periodic blade using the RSM turbulence model.
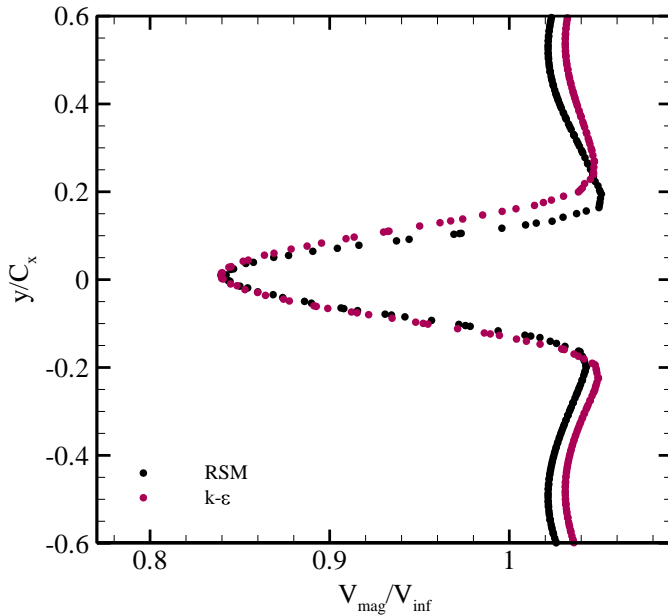

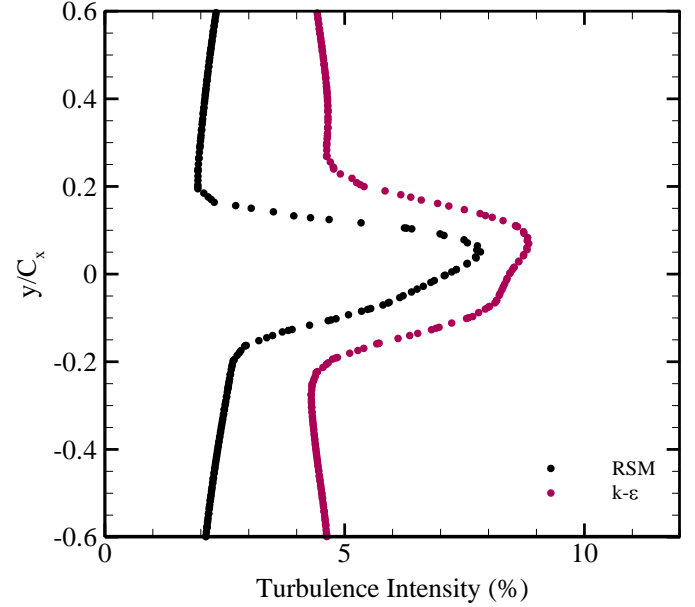**Figure 7. Velocity profile in the blade wake ($x/C_x = 3.0$) as predicted by the RSM and k-ε turbulence models.**

Figure 8. Turbulence intensity in the blade wake ($x/C_x = 3.0$) as predicted by the RSM and k-ε turbulence models.

Cylinder

The computational domain consisted of a single cylinder with periodic conditions imposed at approximately the mid-passage, as seen in Figure 9. Near the blade, a structured quad mesh was generated to capture the boundary layer, shown in Figure 9. The mesh consisted of 40,000 cells with the majority of the cells located around the cylinder and in the cylinder wake.

The cylinder solution shows that the boundary layer and separation are both laminar, with the transition to turbulence occurring in the wake. The von Karman street can also be seen in the solution, in Figure 10. This will have a distinct effect on the width of the wake created since time averaged solutions will be used.
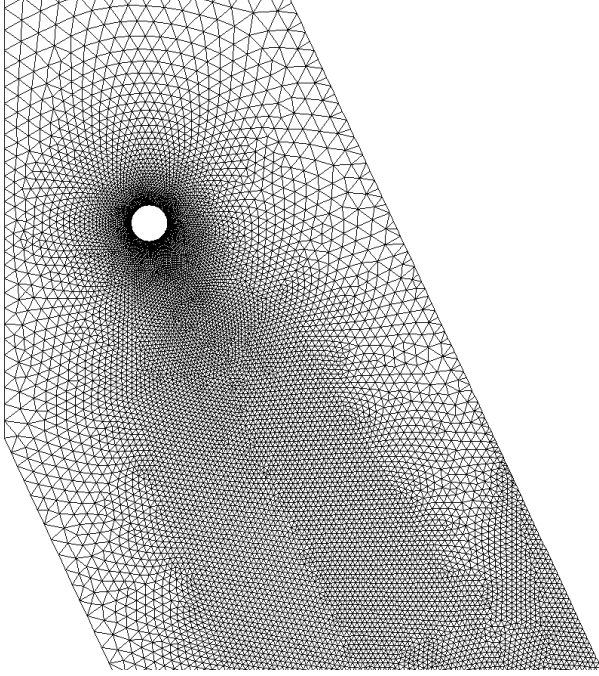
4

Figure 9. Computational domain (left) and representative mesh in the near-wake region of the cylinder (right).

Figure 10. Instantaneous iso-surfaces of constant vorticity magnitude in the wake of the circular cylinder. Surfaces are colored by pressure.

Comparison

Results for a 6mm cylinder (currently used in the tunnel) are shown first, Figure 11. At x/d=8, where x is the distance downstream from the cylinder and d is the diameter, the velocity deficit is comparable. However, even at this point the width of the wake is

slightly too large. As for the turbulence intensity, at x/d=8 the levels are much too high. The peak levels don't drop to the blade wake levels until x/d=16. It is apparent, however, that the width of the turbulent rise is too large, Figure 12.
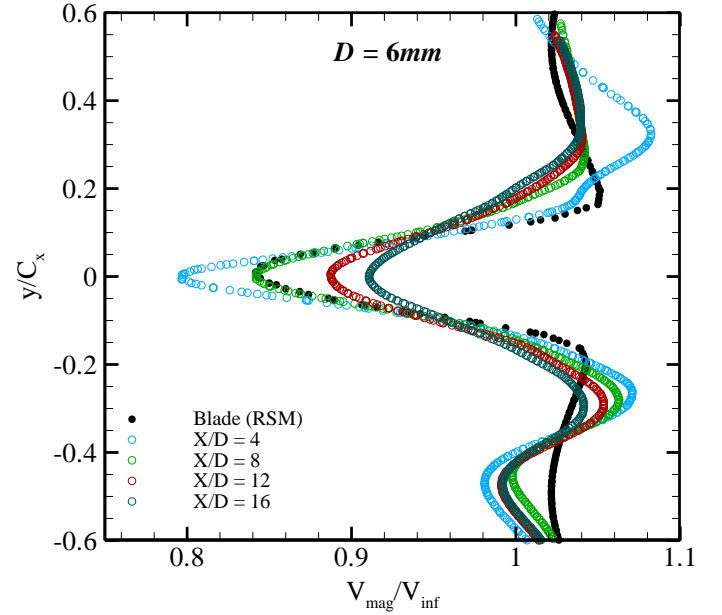

Figure 11. Comparison of the velocity profile in the blade wake at $x/C_x = 3.0$ with the wake behind a 6 mm circular cylinder at various downstream locations.
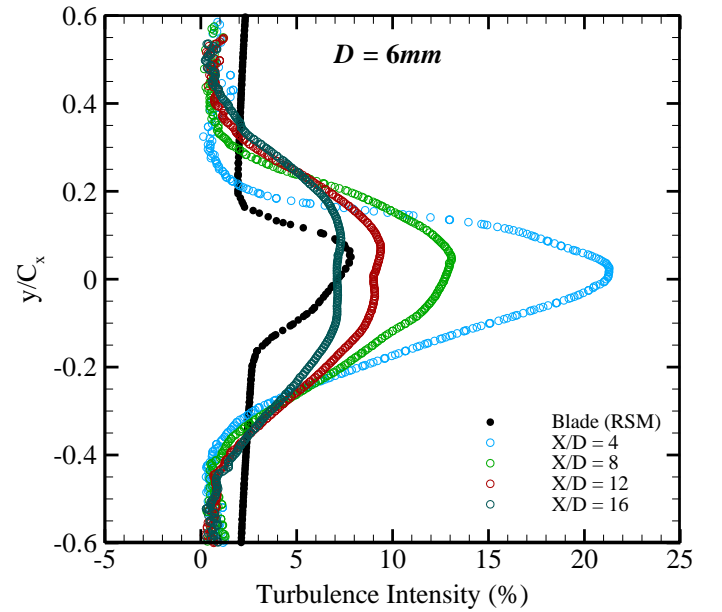

Figure 12. Comparison of the turbulence intensity in the blade wake at $x/C_x = 3.0$ with the wake behind a 6 mm circular cylinder at various downstream locations.

5

By reducing the cylinder diameter to 4mm we can reduce the width of the wake. In Figure 14 we see that in terms of velocity deficit only, the 4mm cylinder at x/D=8 approximates very well the blade wake. However, we see that the problem regarding the turbulence intensity has not been fully resolved.

Based on these simulations, we selected a 4mm cylinder at x/D=8 as the most appropriate solution using simple circular cylinders.

Figure 13. Comparison of the velocity profile in the blade wake at $x/C_x = 3.0$ with the wake behind a 6 mm circular cylinder at various downstream locations.
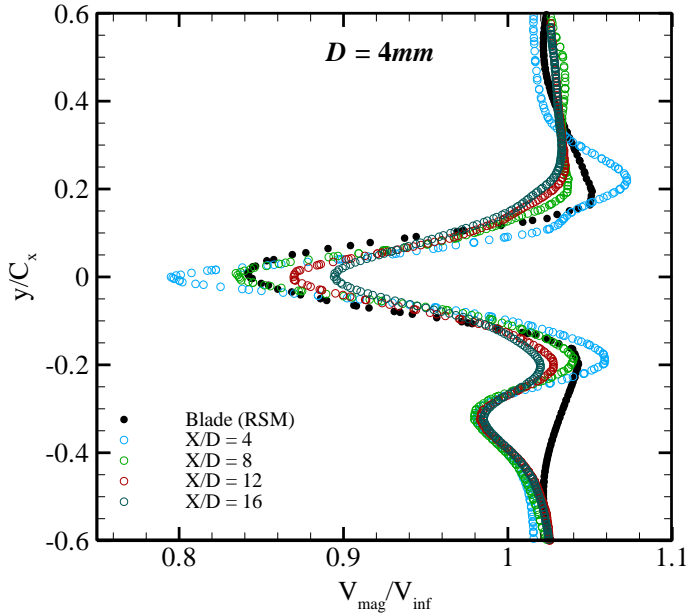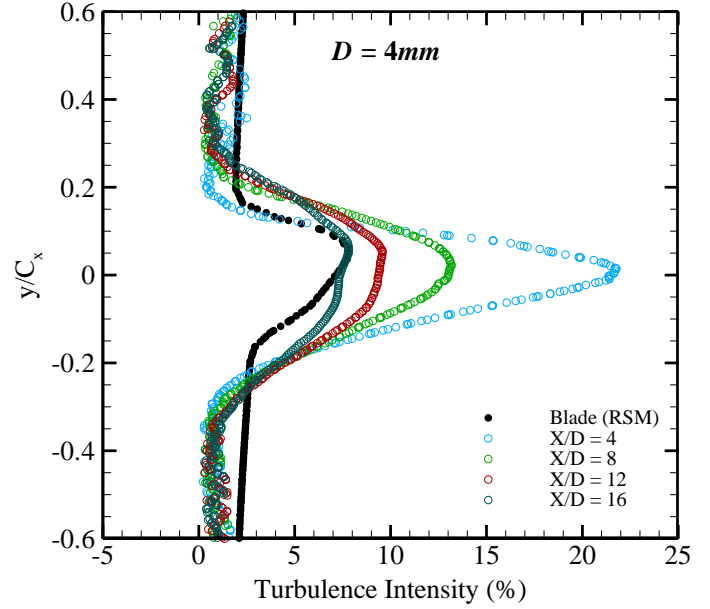

Figure 14. Comparison of the velocity profile in the blade wake at $x/C_x = 3.0$ with the wake behind a 6 mm circular cylinder at various downstream locations.

2. LES Comparison with Experiment

I. Motivation

Active flow controls such as vortex generating jets (VGJs) have been shown to successfully manage laminar separation and hold promise because of the potential to be adjusted during operation, depending on mission conditions. In light of the numerous variables influencing VGJ performance, ranging from (and not limited to) jet on-time duration and velocity to orientation relative to the free stream, it becomes clear that application of VGJs is a complex problem. High resolution numerical studies can potentially shed light on interactions between these and other complex factors inherent to these flow controls.

Experiments conducted by Hansen and Bons[12, 13] evaluated various VGJ settings on a flat plate using particle image velocimetry (PIV) at a Reynolds number based on plate length of 50,000. The main objective of these experiments was to observe the formation of vortical structures downstream of the jet, subjected to both zero and adverse pressure gradients, and evaluate their effect on laminar separation reduction. These experiments provide well-defined geometries and flow conditions with which to benchmark numerical simulations of VGJs by an in-house hybrid solver, which was the primary goal of this work. Three flow conditions from the experimental study were simulated numerically. First, simulations of steady-blowing, angled VGJs on a flat plate under a zero pressure gradient (ZPG) were compared directly against time-averaged experimental data. Then, pulsing capability for the angled VGJ was demonstrated in the ZPG flow field, though only a brief qualitative comparison between averaged experimental data and instantaneous numerical data was performed. An adverse pressure gradient (APG) was then applied to the flat plate to achieve a laminar separation zone comparable to that found on a LPT blade. An analysis of flow features appearing in the numerical results is discussed followed by a qualitative comparison with the experimental results of the interaction between the jet fluid and the separation zone.

II. Experimental Setup

The following is a brief description of the experimental setup utilized by Hansen and Bons.[12] Detailed descriptions of the experimental configuration and equipment can be found in Hansen.[13] The open circuit wind tunnel used in the experiments has a 0.381 m x 0.381 m x 1.83 m test section, constructed of clear acrylic plastic to provide internal views for optical flow measurement techniques. Various flow treatments are applied upstream of the testsection, reducing freestream turbulence levels to less than 0.5%. The angled VGJ holes are 4 mm x 8 mm ovals at the surface. They are also angled 90± to the free stream at a pitch angle of 30± from the *xz* plane, as shown in Figure 1 which depicts a hypothetical VGJ configuration just upstream of the separation

zone on a LPT blade. In the experimental study, the spanwise row of holes was placed 0.36 m from the leading edge of the °at plate and each hole spaced 10 diameters from its nearest neighbor, as shown in Figure 2. Reynolds number based on *x* distance from the leading edge of the plate to the VGJ row and inlet velocity was 50,000.
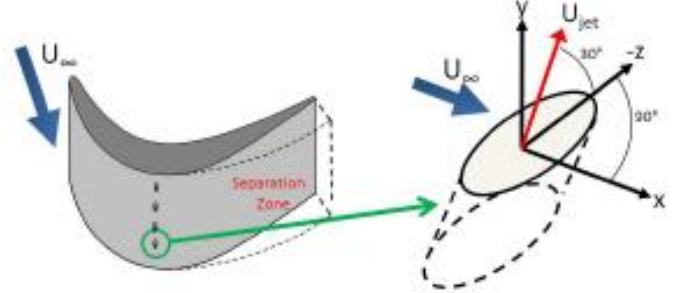

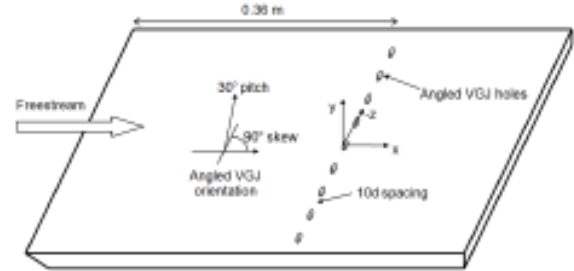**Figure 1. Schematic of VGJ hole in hypothetical LPT application.**

Figure 2. Schematic of flat plate configuration, showing flow and jet direction relative to free stream. Modified from Hansen.
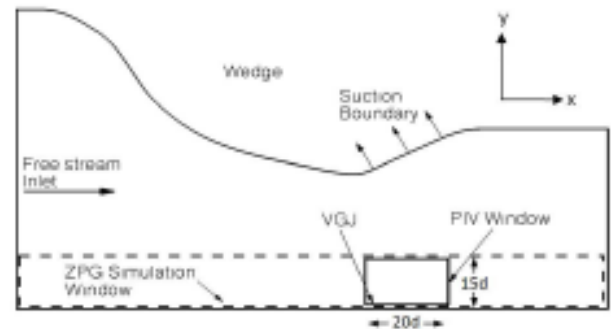
Figure 3. Side view of wedge configuration showing suction boundary and data windows for PIV measurements and ZPG numerical simulations. APG simulations encompassed entire domain. (Not to scale)

To obtain a laminar separation zone on the flat plate, an adverse pressure gradient was induced by inserting a foam wedge on the wall opposite the VGJ plate, as shown in Figure 3. The wedge con⁻guration is similar to that used by Volino and Hultgren1 and simulates the pressure gradient found on the suction surface of a PackB LPT airfoil. It was observed that flow passing through the channel separated at the throat, which interfered with the flow field on the flat plate. This separation was eliminated by first, covering the wall upstream

of the throat with sand paper in an attempt to transition the boundary layer to turbulent and second, by pulling suction aft of the throat. The desired pressure distribution was found by iterating on suction strength. Stereo three-component particle image velocimetry (PIV) measurements were obtained by illuminating two dimensional slices of the flow field with a green Nd:YAG laser sheet oriented perpendicular to the plate in the xy plane. The flow field for one hole pitch was obtained by measuring the velocity fields at 21 domain slices spaced 2 mm in the spanwise direction. These velocity planes (containing all three velocity components) were combined into a three-dimensional flow field using Matlab. Velocity uncertainty was estimated at 0.1 m/s based on a seed particle position uncertainty of 0.1 image pixels, as declared by the software vendor.

Jet configuration settings were specified as follows. The jet exit velocity is typically represented in terms of a blowing ratio, B, which is defined as the ratio of the jet exit velocity to the freestream velocity above the jet hole. Bons et al.[4, 5] found that a blowing ratio between 2 and 4 was effective for separation reduction. The lower end of this range was selected in order to minimize compressed air requirements to the tunnel. Three blowing ratios were evaluated in these experiments. The steady ZPG case was set to B=2 and increased to B=2.5 when pulsed, and the pulsed APG case was conducted at B=3. The pulsing frequency for both pressure gradient settings was set to 5 Hz at a duty cycle (ratio of jet on time to pulse period) of 25%. An example pulse, normalized by the time of a complete pulse period T, is shown in Figure 4. In this case a duty cycle of 25% is shown for a maximum blowing ratio of 3. The dashed line represents the step function utilized in the numerical simulations. In order to analyze specific points in time during the pulse profile, a phase-locked averaging method was utilized. Discrete points in the pulse period, referred to as phases, were chosen to observe VGJ behavior during pulse-on time (phases 1-3) and at various points in time after the jet had switched off (phases 4-8). Instantaneous flow fields were recorded at each phase, as indicated in time by the numbered arrows, for 40 pulse periods. An average flow field at each phase was then created from these instantaneous data.

III. Numerical Method

A time-accurate hybrid LES/DNS solver was chosen for the VGJ simulations. It solves the unsteady, incompressible Navier Stokes equations using a second order Finite element method in the xy plane and a Fourier method in the spanwise (or z) direction. This method lends well to solving flow fields around two-dimensional geometries that are characterized by spanwise-periodic, three-dimensional flow features. For detailed descriptions of the solver formulation, the reader is directed to Snyder and Degrez.[14, 15] Temporal discretization of the equations consists of a second-order accurate Adams-Bashforth method for the convective terms and a second order accurate Crank-Nicolson method for the diffusion and

pressure terms. The solver has been successfully validated against various classic fluid flows.[14-16]

The Fourier formulation utilizes a single two-dimensional unstructured mesh for the solution of each Fourier mode. The modes are resolved at each global time step and the three-dimensional flow field is obtained upon taking the inverse discrete Fourier transform of all the modes. Signal aliasing in the solution is eliminated by only computing half of the total Fourier modes. Decoupling of the Fourier modes, also resulting from the formulation method, readily facilitates parallel computing configurations.
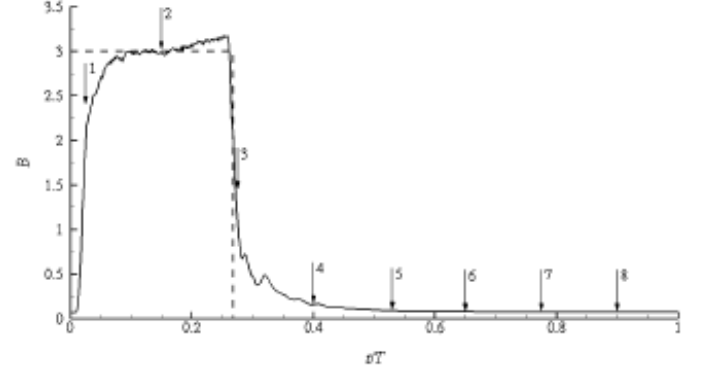

Figure 4. Plot of experimental pulse history and individual phase locations. Dashed line represents corresponding numerical pulse step function.

The VGJ hole was simulated by creating a boundary condition which specifies a Fourier approximation of the hole velocity distribution in the spanwise direction. Though experimental velocity profiles at the hole exit were measured, a step function was deemed sufficient for this work. Pulsing parameters (frequency and duty cycle) were also factored into the boundary condition. As shown in Figure 4, the pulse cycle was approximated as a step function as opposed to using the experimental pulse profile. The simulations of the APG domain were performed with the unstructured mesh shown in Figure 5. The mesh domain retains the experimental geometry scale but only extends 0.24 m downstream of the VGJ hole. Also shown in the figure are the locations and types of non-wall boundary conditions. The use of a Fourier method in the spanwise direction necessitates a periodic boundary condition in that direction (into the page). This requirement lends well to the experimental configuration described previously, which consists of a spanwise row of holes. Not shown in this figure is a coarsly meshed viscous dissipation zone added downstream of the mesh as shown. This was applied to allow spanwise vortical structures from the laminar separation zone to dissipate before arriving at the outflow boundary, whose passage induced solver instability. Table 1 describes the two meshes utilized for these simulations.
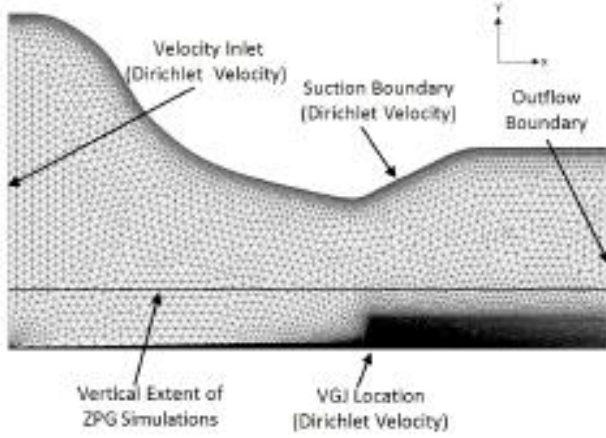
8

Figure 5. 2-D mesh utilized for APG simulations showing non-wall boundary conditions.

The resolution surrounding the VGJ was increased for the ZPG case and overall cell count (and thus computation time) was controlled by eliminating the wedge and restricting the domain to a height of y/d=15 above the wall. This is indicated by the horizontal black line crossing the domain slightly above the plate wall in Figure 5. This horizontal boundary in the ZPG case was set to an outflow. The vortex dissipation zone was not needed for the ZPG cases. The CFL number noted in the table represents the maximum value found in the domain based on the local cell velocity, characteristic cell length, and the global time step, though the calculation excludes the presence of the VGJ. The reduced boundary layer parameter, $y+$, is the maximum value found on the plate wall upstream of the VGJ hole. The grid sizes indicated were the result of a mesh resolution study involving both the total Fourier mode count and the node resolution at the VGJ hole. The unstructured meshes were created such that increased cell density could be located in regions surrounding areas of interest, such as boundary layer growth upstream of the VGJ and the flow field in direct vicinity of the jet wake. Lastly, though the LES turbulence model was available in the solver, it was not utilized in any of the simulations.

Table 1. Statistics for unstructured meshes used for ZPG and APG cases.

Node Resolution at VGJ in x direction	Cell Count for 256 Fourrier Modes	CFL number $(u\Delta t/\Delta x)$ without VGJ	y^+
0.15 mm (APG)	15,300,000	0.3	1.0
0.1 mm (ZPG)	15,600,000	0.4	0.5

IV. Steady VGJ in Zero Pressure Gradient

Prior to implementing the VGJ, the Reynolds number based on momentum thickness at the VGJ hole was measured for the no-control case. A value of 135 was obtained from the numerical results, which is within 11% of the experimental

value of 150. This indicates sufficient growth of the numerical boundary layer while remaining below the critical value of 200 at which unsteady fluctuations no longer dissipate as they convect downstream.
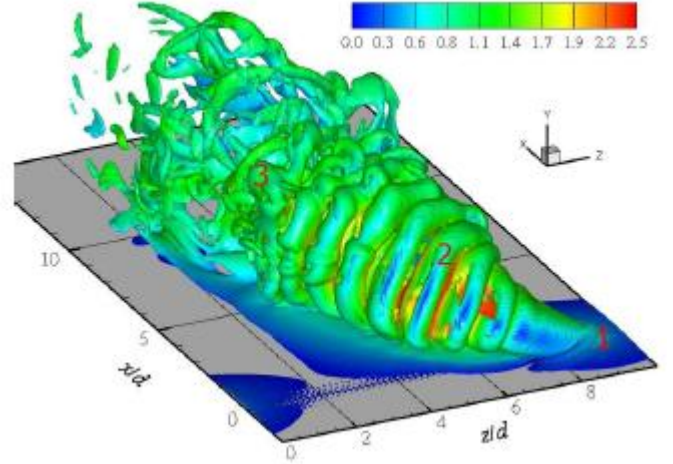

Figure 6. Iso-surfaces of instantaneous vorticity magnitude, $\omega_{mag}d/U_\infty$=2, colored by velocity magnitude.

The VGJ was enabled at a blowing ratio of 2 from the no-control case and an instantaneous view of the jet is shown in Figure 6. In this plot, the VGJ is located at x/d =0 and z/d =8.5 and is firing in the $-z/d$ direction. A small spanwise vortex can be seen forming at the base of the jet fluid column near the wall (1). This vortex represents a roll-up of the boundary layer upon encountering the jet column, which effectively acts as a solid object to the oncoming freestream. The well defined vortical rings visible in the plot are the result of shear layer roll-up due to the velocity gradient existing between the jet fluid and the freestream (2). These rings do not wrap entirely around to the leeward side of the jet fluid. This asymmetry exists because of the same solid blockage effect inducing the boundary layer roll-up vortex. In other words, the freestream is blocked from interacting with the jet fluid directly downstream of the hole and thus a lower velocity gradient exists, which is insufficient to produce the vortex rings. These vortex rings dissipate around x/d =5 and the flow is then characterized by turbulent wake (3). The rings agree with vortical features observed in flow visualization experiments performed by various researchers on wall-normal cross-flow jets.[17-19] The rings were labeled kidney vortices (because of the radial cross-sectional shape of the rings) and were observed in various forms ranging from pairs to multiple pair formations. Further analysis of the numerical results show that they are characterized by a high core vorticity and are also observed forming in pairs (not shown) before breaking down to turbulence. The dissipation to turbulence was also noted in the flow visualizations. The solver was then configured to record a time average to compare average vortical structure formation with average PIV data. Averages were conducted for 8 s of flow time, or just over 13 flow passages through the

domain. Contour plots of normalized streamwise velocity at various cross-flow cutting planes are shown in Figure 7.
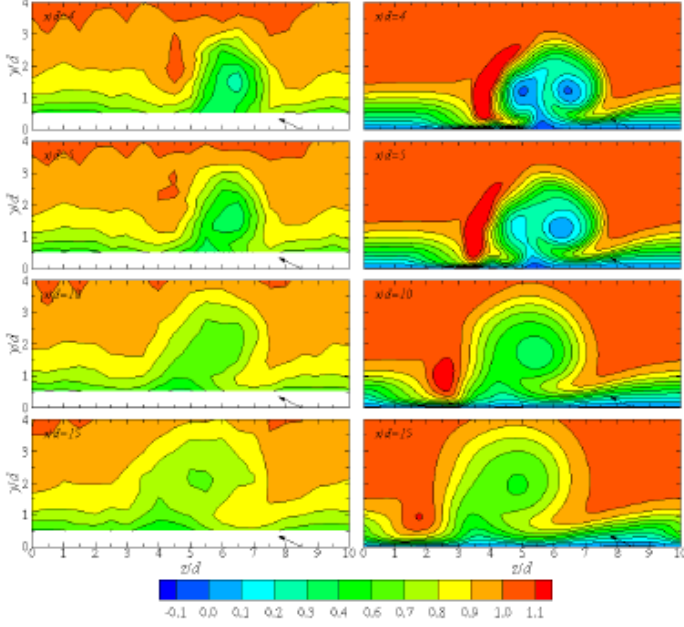

Figure 7. Contours of average experimental and numerical streamwise velocity, u/U_∞, at various x/d planes. Experiment in left column.

The flow field is dominated by a lobe of low-momentum freestream which spreads in the spanwise direction as it propogates downstream. This momentum deficit also coincides with the location of the large vortex core which is characteristic of an angled cross-flow jet. The deficit is primarily due to freestream blockage by the jet fluid. Vortical mixing of high momentum freestream fluid with low momentum boundary layer fluid is visible by a dip in the boundary layer region to the right of the lobe. An acceleration zone exists directly to the left of the lobe, which coincides with the passage region of the kidney vortices. This acceleration is possibly a combination of an increase in velocity induced by the high core vorticity of the kidney vortices and an acceleration of the freestream fluid around the 'solid' jet fluid. These figures indicate good agreement between the experiments and the numerical results.

Figure 8 shows contours of normalized streamwise vorticity at the same x/d locations in Figure 7. The presence of the primary vortex is clearly visible in addition to the spanwise spreading which occurs as the core dissipates downstream. Also visible in both plots is an arch extending over the top of the primary vortex possessing a positive vortical component. This arch is the time-averaged passage region of the kidney vortices. The thin negative vorticity region just below the positive arch indicates the passage region of the second vortex in the kidney vortex pair. The significantly weaker arch visible in the experiments is largely due to the lower spatial resolution of the experimental data as compared to the numerical

simulation (an order of magnitude difference in the spanwise direction). Furthermore, experiments conducted by Bloxham et al. utilzing slightly different PIV data acquisition methods with the same experimental configuration, show a stronger arch for these same flow conditions.[20]
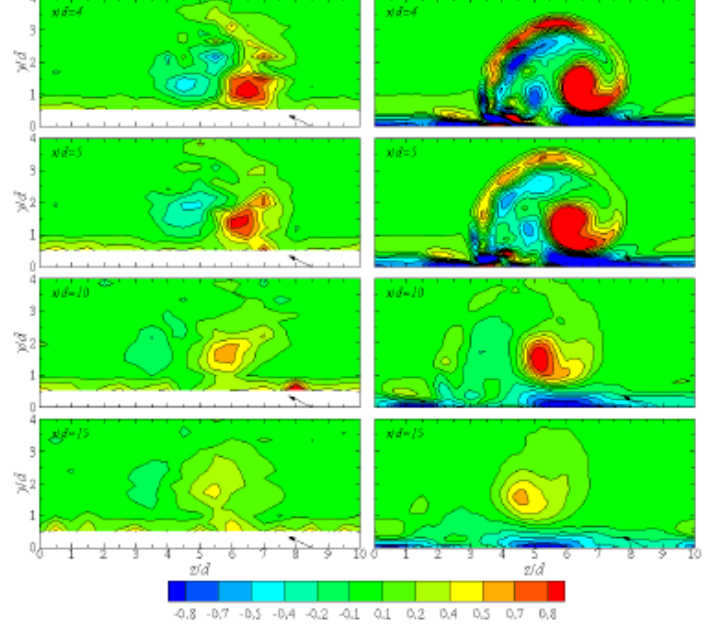

Figure 8. Contours of average experimental and numerical streamwise velocity, $\omega_x d/U_\infty$, at various x/d planes. Experiment in left column.

Overall, though the numerical vortical core drifts slightly more in the spanwise direction, the results compare well with the experimental data. These plots point to the presence of two distinct regions in the flow field. The first is a formation region which extends downstream to $x/d =5$ and is characterized by a variety of vortical structures in addition to the developing primary vortex such as a smaller and weaker secondary vortex to the left of the primary core (already dissipated at $x/d =4$), the kidney vortex rings, and other smaller vortical structures surrounding the developing primary core. The second region extends downstream to the end of the domain. In this region the primary vortex has enveloped the neighboring structures and spatially dominates the flow as it dissipates.

V. Pulsed VGJ in Adverse Pressure Gradient

Pulsing was then initiated from the no-control case at a frequency of 2 Hz and a duty cycle of 25%. Numerical phase-lock averaging was performed identically to the experimental method to analyze and compare discrete points in the pulse history. However, the phase- lock averaged numerical flow fields were largely identical to the instantaneous flow fields from which they were calculated. This is due to a lack of

experimental pulse to pulse variations in the numerical simulations. Factors contributing to these variations consist of varying seed concentration passing through the PIV data acquisition plane, variations in the pulsing mechanism, or general freestream fluctuations. Another factor playing a role is the use of a step function to simulate the VGJ hole. The numerical scheme did not factor in boundary layer or vorticity levels that would exist in the experimental jet exit profile. Lastly, though secondary in nature compared to the variations just mentioned, the PIV system requires a pair of sequential images in order to obtain an instantaneous velocity vector field at each phase. The difference in time between these images creates a slight temporal average that is not accounted for in the numerics. Thus, the contour plots shown in Figure 9 show a qualitative comparison between the averaged experimental data and the instantaneous numerical data at the same locations in the pulse history. These plots demonstrate the time-accuracy of the numerical solver in that the bulk jet fluid is seen convecting downstream of the hole the same distance as the experiments. It is not unreasonable to assume that upon including the above experimental factors into the numerical simulations, the average of the flow structures visible in the numerics would likely reveal a flow field much more similar to the experimental results.

VI. Pulsed VGJ in Adverse Pressure Gradient

As in the ZPG simulations, a no-control case was evaluated to compare the numerical laminar separation zone to the experimental results. The pressure distribution is shown in Figure 10 where Cp is defined as $1 - (Ue/Uex)^2$. The boundary layer edge velocity, Ue, was acquired by traversing the domain in the streamwise direction at a height of $y/d = 15$ above the flat plate and Uex is the velocity at the channel exit. The numerical results compare favorably to the experimental values as well as a separate numerical study performed by Volino and Hultgren.[1] Separation location in the streamwise direction was measured based on the first zero crossing of the spanwise-averaged wall shear stress plot. The numerical pressure gradient was found iteratively by changing the Dirichlet velocity setting at the suction boundary and observing the point of separation relative to the VGJ holes. Priority was given to the x/d separation location in an attempt to simulate the momentum level of the jet fluid relative to the separation zone. Table 2 compares experimental and numerical separation zone dimensions, with good agreement.
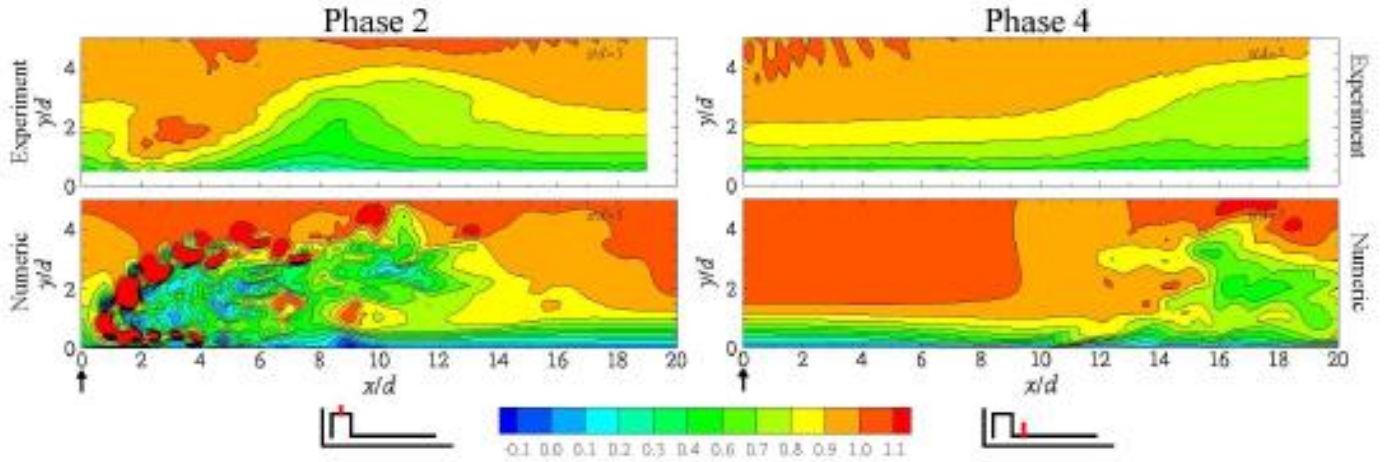

Figure 9. Contours of average experimental and instantaneous numerical streamwise velocity, u/U_∞, at z/d=5, for phases 2 and 4. Jet location indicated by black arrows, firing into page.

Figure 11 shows iso-surfaces of the no-control separation zone. The flow is moving in the positive x/d direction and the jet is again located at $x/d = 0$ and $z/d = 8.5$. The zone remains laminar passing through the PIV data window ($x/d = 20$) which is consistent with the experimental observations, and transitions to turbulent at $x/d = 40$.

Figure 12 plots iso-surfaces of vorticity magnitude showing the jet fluid exiting the hole when subjected to the adverse pressure gradient. Distortion of the jet fluid structure due to the APG is visible at various points in the domain when compared to Figure 6. The boundary layer roll-up vortex at the base of the fluid column is wider in the spanwise direction (1). The kidney vortex rings form closer to the VGJ hole but do

not posess the same coherent structure found in the ZPG cases (2). The rings and wake dissipate to turbulent flow much sooner as they convect downstream of the hole (3). Lastly, the pressure gradient stretches the wake taller and wider than is observed with no pressure gradient (4). The increase in spanwise spread can be noted by the iso-surfaces appearing in the domain at $x/d = 10$ and $z/d = 10$. Recalling the spanwise periodic boundary condition of the boundaries lying in the xy plane, these vortical strucures are the wake of the neighboring jet. By comparison, the neighboring jet wake does not appear in the domain until further downstream, in the ZPG cases.
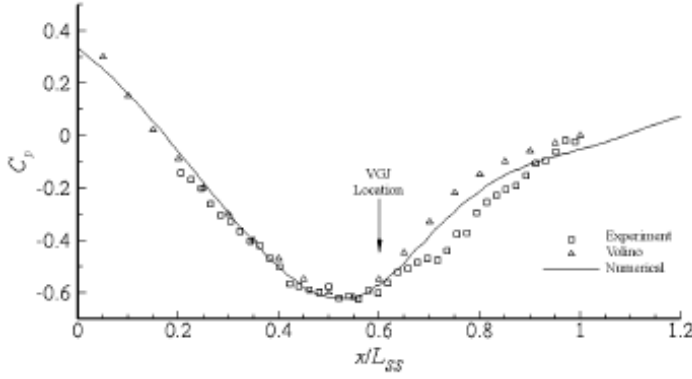
Figure 10. Pressure coefficient distribution for APG simulations.

Table 2. Laminar separation zone dimensions.

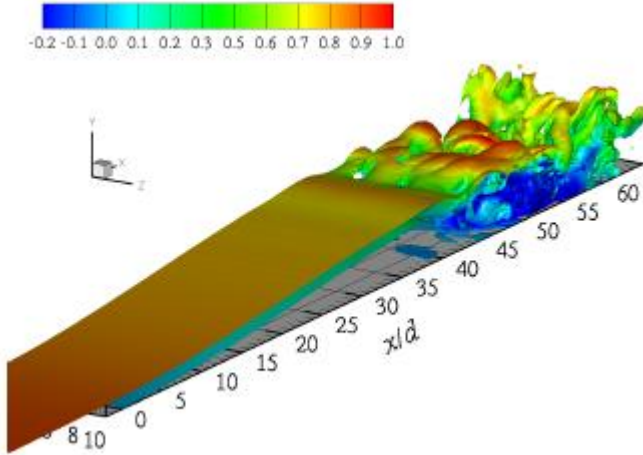|	Separation Pt	$u_\infty=0.5$ at x/d=20	$u_\infty=0.9$ at x/d=20
Experimental	x/d=6.0	y/d=2.2	y/d=4.4
Numerical	x/d=5.7	y/d=2.6	y/d=3.4

Figure 11. Instantaneous iso-surfaces of numerical vorticity magnitude, $\omega_{mag}d/U_\infty$=0.6, colored with streamwise velocity for no-control APG case.

Two separation reduction scenarios will now be discussed: jet fluid interaction with an undisturbed separation zone (first pulse) and jet fluid interaction with a controlled separation zone (subsequent pulses). The jet pulsing was initialized at a duty cycle of 25% and is shown in the contour plots of spanwise vorticity in Figure 13. These plots were taken along a cutting plane oriented parallel to the freestream at z/d =4 (for reference, recall the jet hole center is at z/d =8.5). At t/T =0, the separation zone is at the state shown in Figure 11, where the diagonal strip of negative vorticity is the free shear layer of the separation zone. By t/T =0.12, the section of the free shear layer between x/d =15 and 20 has begun to distort. This distortion occurs independently of the leading packet of jet fluid which has passed over the top of the separation zone. By t/T =0.15 a well defined negative vortical structure has

formed, as indicated by the red arrow. Noting that this roll-up appears to be independent of the initial impact of the jet fluid and that the formation occurs relatively rapidly, it likely results from an abrupt change in the upstream separation zone. Indeed, the separation layer directly downstream of the jet hole experiences a spanwise flattening effect directly downstream of the hole. At t/T =0.18 a second shear layer vortex is visible downstream of the first. By t/T =0.24 these shear layer vortices have dissipated and the shear layer structure has been largely eliminated. The remainder of the separation zone is flushed out of the domain by the jet fluid and the freestream. By the time the next jet pulse is to begin (t/T =0.99), the separation zone is observed regrowing (x/d =25 to 30) but does not fully return to its pre-pulse height and strength. This lack of re-growth was also observed experimentally. Numerical re-growth levels are within 80% of the experimental regrowth level of 50% of the no-control height. In both the numerical and experimental results, re-growth was measured based on freestream velocity profiles in the wall-normal direction at the x/d =20 location.
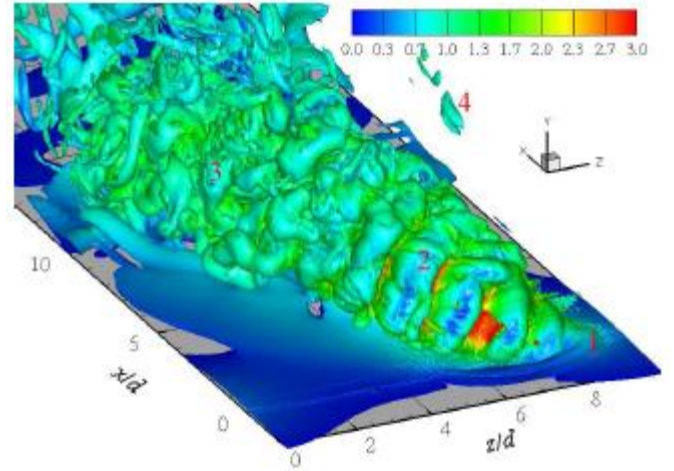

Figure 12. Instantaneous iso-surface of numerical vorticity magnitude, $\omega_{mag}d/U_\infty$=2, colored with velocity magnitude for APG case.

Though only one numerical follow-up pulse was recorded after this initial pulse, agreement with the experimental separation zone re-growth level suggests that the weakened numerical separation zone would return to this same height at the end of subsequent pulses.

Subsequent pulses of the jet interact with this significantly reduced laminar separation zone. Figure 14 shows iso-surfaces of streamwise velocity at phases 2 and 3 in the pulse history. These plots compare phase-lock averaged experimental data with instantaneous numerical data as was performed for the ZPG case. The reader should note that the numerical iso-surfaces are for a normalized streamwise velocity component of 0.5 whereas the experimental surfaces are for 0.6. This was done to increase the visible surface of the experimental data for a better comparison and creates negligible differences

between the plots. The jet fluid in phase 2 is seen rising above the separation zone with the same general trajectory. The separation zone directly below the jet plume has undergone the spanwise flattening mentioned previously. The streamwise extent of the numerical flattened zone agrees well with the experimental results. Though the iso-surface representing the jet fluid does not extend as far downstream in the experimental results, a trough developing in the streamwise direction through the separation zone would likely be the result of jet fluid passing above, as observed in the numerical results. By phase 3, the jet has just switched off and with the exception of remnants of the separation zone at $x/d = 20$, the

separated fluid has been almost entirely flushed out of the data window. The spanwise shear layer vortices observed in the numerical results for the initial pulse were also observed in the follow-up pulses. However, due to the reduced size of the separation zone, less low-momentum fluid is available to create vortices of the same magnitude and size observed in the initial pulse. This reduction in size is also the result of reduction in shear layer proximity to the plate wall. Overall, general trends of the interaction between the simulated jet with the separation zone agrees with the experimental data.
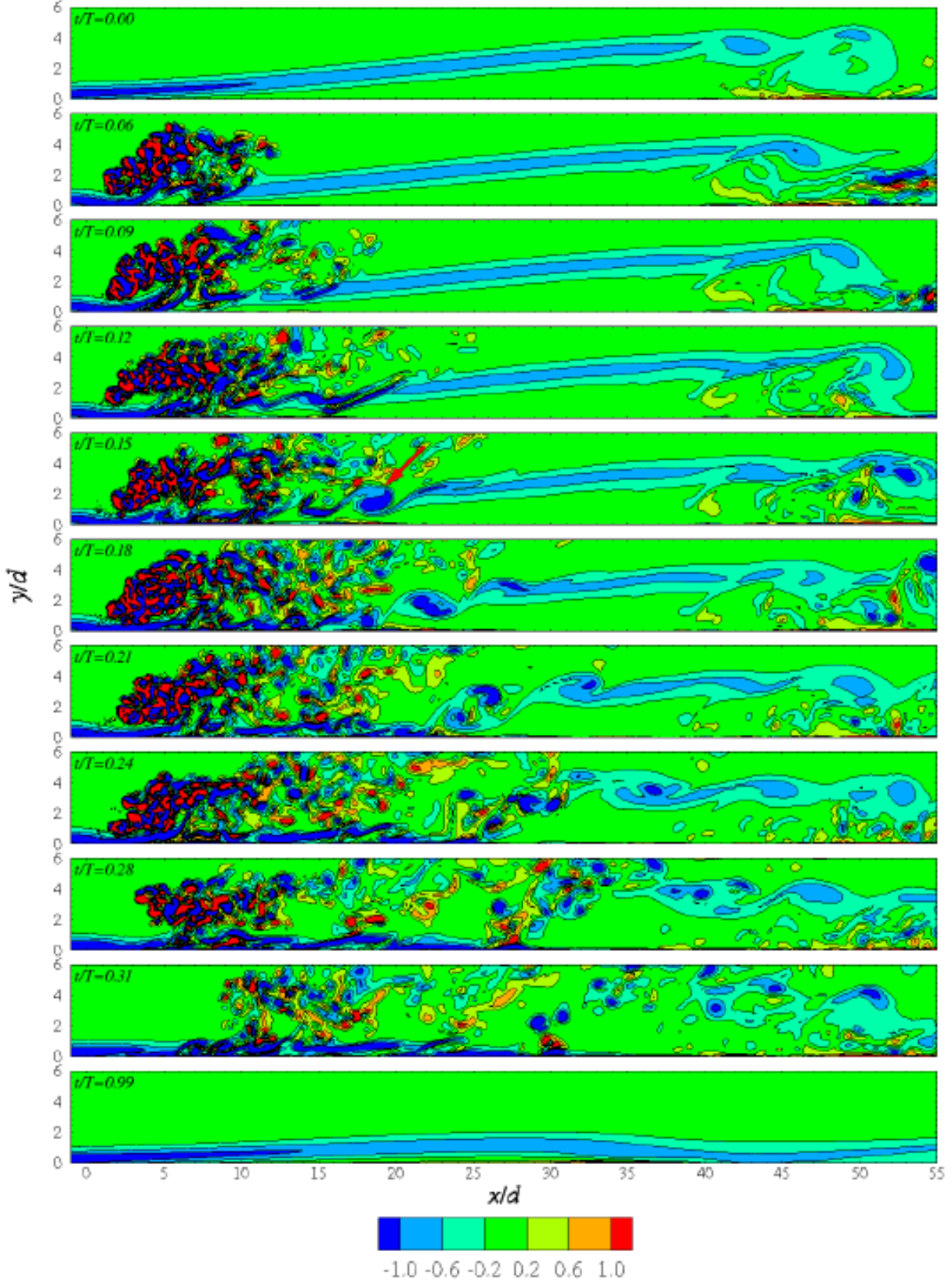
Figure 13. Instantaneous contour plots of numerical spanwise vorticity, $\omega_x d/U_\infty$ at z/d=4, showing various points in APG pulse period for the undisturbed separation zone.
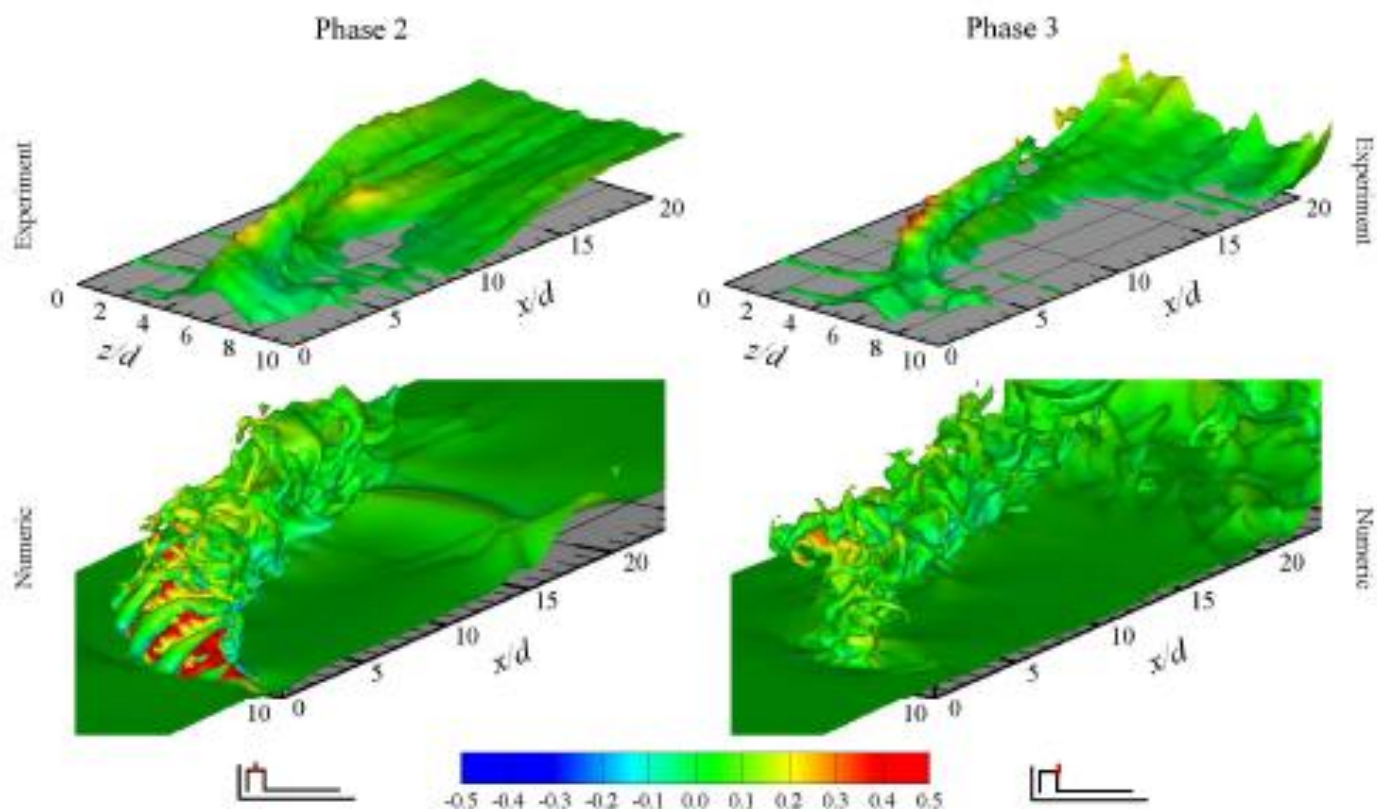
14

Figure 14. Average iso-surfaces of experimental streamwise velocity, u/U_∞=0.6, and instantaneous iso-surfaces of numerical streamwise velocity, u/U_∞=0.5 colored with wall-normal velocity at phases 2 and 3.

References

1) Volino, R. J. and Hultgren, L. S., "Measurements in Separated and Transitional Boundary Layers Under Low-Pressure Turbine Airfoil Conditions," *ASME Journal of Turbomachinery*, Vol. 123, No. 2, 2001, pp. 189-197.

2) Yuan, L. L., Street, R. L., and Ferziger, J. H., "Large Eddy Simulations of a Round Jet in Crossflow," *Journal of Fluid Mechanics*, Vol. 379, 1999, pp. 71-104.

3) Jiang, L. and Liu, C., "Direct Numerical Simulation for Flow Separation Control with Pulsed Jets," *41st AIAA Aerospace Sciences Meeting and Exhibit*, January, 2003, Reno, NV AIAA 2003-0611, pp. 1-33.

4) Bons, J., Sondergaard, R., and Rivir, R. B., "Turbine Separation Control Using Pulsed Vortex Generator Jets," *Transactions of the ASME*, Vol. 123, April 2001, pp. 198-206.

5) Bons, J., Sondergaard, R., and Rivir, R., "The Fluid Dynamics of LPT Blade Separation Control Using Pulsed Jets," *Journal of Turbomachinery*, Vol. 124, January 2002, pp. 77-85.

6) Bloxham, M., Reimann, D., and Bons, J. P., "The Effect of VGJ Pulse Characteristics on Separation Bubble Dynamics," *44th AIAA Aerospace Sciences Meeting and Exhibit*, January, 2006, Reno, NV 2006, pp. 1-14.

7) Rizzetta, D. P. and Visbal, M. R., "Numerical Simulation of Separation Control for a Transitional Highly-Loaded Low-Pressure Turbine," *2nd AIAA Flow Control Conference*, June 2004, Portland, Oregon 2004-2204, pp. 1-24.

8) Postl, D., Gross, A., and Fasel, H. F., "Numerical Investigation of Low-Pressure Turbine Blade Separation Control," *41st AIAA Aerospace Sciences Meeting and Exhibit*, January, 2003, Reno, NV AIAA 2003-0614, pp. 1-12.

9) Postl, D., Gross, A., and Fasel, H., "Numerical Investigation of Active Flow Control for Low-Pressure Turbine Blade Separation," *42nd AIAA Aerospace Sciences Meeting and Exhibit*, January, 2004, Reno, NV AIAA 2004-0750, pp. 1-13.

10) Gross, A. and Fasel, H. F., "Simulation of Active Flow Control for a Low Pressure Turbine Blade Cascade," *43rd AIAA Aerospace Sciences Meeting and Exhibit*, January, 2003, Reno, NV AIAA 2005-0869, pp. 1-18.

11) Gross, A. and Fasel, H., "Investigation of Low-Pressure Turbine Separation Control," *45th AIAA Aerospace Sciences Meeting and Exhibit*, January, 2007, Reno, NV AIAA 2007-0520, pp. 1-15.

12) Hansen, L. and Bons, J., "Phase-Locked Flow Measurements of Unsteady Vortex Generator Jets in Separating Boundary Layer," *Journal of Propulsion and Power*, Vol. 22, No. 3, May 2006, pp. 558-566.

13) Hansen, L., "*Phase Locked Flow Measurements of Steady and Unsteady Vortex Generator Jets in a Separating Boundary Layer"*, Masters thesis, Brigham Young University, April 2005.

14) Snyder, D. O. and Degrez, G., "Large Eddy Simulation With Complex 2-D Geometries Using a Parallel Finite-Element/Spectral Algorithm," *International Journal for Numerical Methods in Fluids*, Vol. 41, No. 10, 2003, pp. 1119-1135.

15) Snyder, D. O., *A Parallel Finite-Element/Spectral LES Algorithm for Complex Two-Dimensional Geometries*, Ph.D. thesis, Utah State University and Von Karman Institute For Fluid Dynamics, January 2002.

16) Nierhaus, T., Thomas, J., Detandt, Y., and Abeele, D., "Direct numerical simulation of bubbly Taylor-Couette Flow," *Proceedings of the 4th International Conference on Computational Fluid Dynamics*, July 2006, Gent, Belgium.

17) Haven, B. and Kurosaka, M., "Kidney and Anti-Kidney Vorticies in Crossflow Jets," *Journal of Fluid Mechanics*, Vol. 352, 1997, pp. 27-64.

18) Perry, A. and Lim, T., "Coherent Structures in Coflowing Jets and Wakes," *Journal of Fluid Mechanics*, Vol. 88, No. 3, 1978, pp. 451-463.

19) New, T., Lim, T., and Luo, S., "Elliptic jets in crossflow," *Journal of Fluid Mechanics*, Vol. 494, 2003, pp. 119-140.

20) Bloxham, M., Memory, C., and Bons, J. P., "Experimental Measurement of Cross-Plane and In-Plane Vorticity Using Particle Image Velocimetry," *46th AIAA Aerospace Sciences Meeting and Exhibit*, January, 2008, Reno, NV AIAA-2008-0709, pp. 1-14.

3. L1A Cascade Results

Experimental Facility

Figure 1 is a plot of the predicted pressure coefficient distribution for the L1A profile compared to the L1M and Pack B. The inset schematic displays the aft portion of the three blades indicating their respective curvature and solidity. The c_p predictions in Fig. 1 were obtained within the AFRL Turbine Design and Analysis System (TDAAS), which was also used to define the L1A profile.
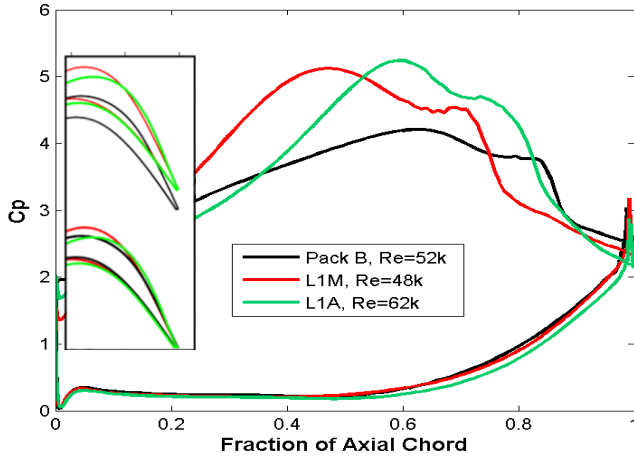

Figure 1: Prediction of c_p for L1A, Pack B, and L1M profiles. Inset shows aft portion of blade profiles.

For a detailed description of the wind tunnel facility refer to Bons et al. [20]. The open-loop wind tunnel is driven by a centrifugal blower. Air flow passes through a series of flow straighteners to enter the inlet duct with ±2% velocity uniformity and 0.3% freestream turbulence. The cascade inlet duct is 1.52 m long with a cross sectional area of 0.239 m. A square-bar turbulence grid is placed 1.35 m ($9.4C_x$) from the inlet plane of the cascade to augment the freestream turbulence to 3% at the inlet plane of the cascade. The cascade has 3 full passages with outer sidewalls and two fully immersed L1A blade profiles (Fig. 2). The L1A blades have an axial chord (C_x) of 0.143 m, a span of 0.38 m, and a solidity of 0.99. The design Zweifel coefficient is 1.34 with a peak c_p at about 58% C_x. At Re=21,000, the L1A blade exhibits a massive separation beginning at approximately 57% C_x and continuing off the trailing edge of the blade. Both blades are equipped with 15 static pressure taps on the suction surface and 7 taps on the pressure surface. The taps are 1mm in diameter and are waterfalled across the middle third of the blade span. These taps are connected to a 0.1 "H_2O Druck pressure transducer to measure the local c_p distribution. The c_p is calculated by taking the inlet total pressure from an upstream pitot-static probe minus the local static pressure and dividing by the inlet dynamic pressure. Uncertainties in the experimental pressure measurements translate to an uncertainty of ±0.10 in the c_p data at Re = 20,000.

The wake generator was positioned 45 mm ($31\%C_x$) upstream of the cascade inlet (Fig. 2). Unsteady wake disturbances are generated using 4mm diameter carbon fiber rods oriented spanwise in the plane parallel to the cascade inlet. The rod diameter and location were selected to simulate the velocity deficit in the wake of an upstream turbine vane with attached boundary layers. The rods are mounted on a chain sprocket system drawn by a variable speed motor. The rod speed was maintained such that the flow coefficient, Φ = 0.76. The rod spacing is 57% larger than the blade spacing. The larger spacing between rods is intended to simulate vane wakes impinging on a rotor blade row since the vane count is typically 60-70% of the blade count for a given LPT stage. Low density foam lining all four sides of the cross-section serves to dampen rod vibrations as well as seal the wind tunnel. An optical sensor signals the exit of each rod from the wind tunnel. For a more detailed description of the wake generator, refer to Bloxham et al.[10].
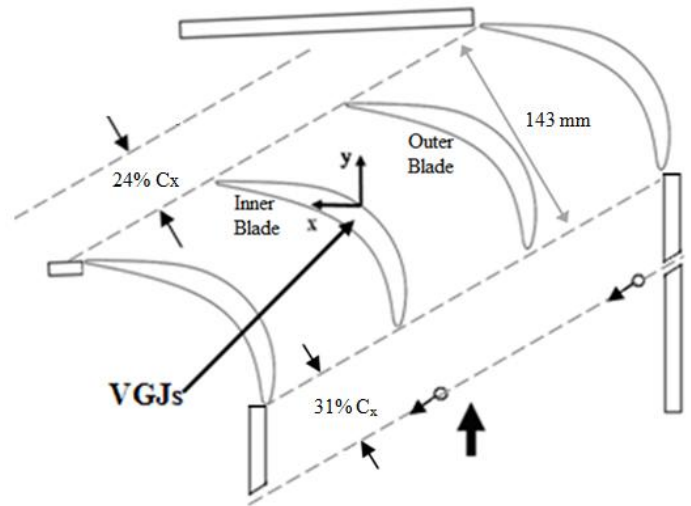

Figure 2: Schematic of L1A linear cascade.

A spanwise plenum (11 mm diameter) located at 59% C_x feeds pressurized air to a spanwise row of vortex generator jets (VGJs) on both blades. The cylindrical jets are 2.6 mm in diameter (d) and are spaced 10d apart. VGJs are typically configured with a low pitch angle and aggressive skew angle to produce a single, dominant, slowly-decaying streamwise vortex. To comply with this, the jet flow is injected at a 30° pitch angle to the blade surface and a 90° skew angle to the streamwise direction. The plenums are connected to high pressure air with an inline Parker-Hannifin high-speed solenoid valve that regulates the VGJ exit velocity. A General Valve Inc. Iota One pulse driver is used to set the duration of the VGJ pulse and the time of actuation relative to the input signal from the rod exit sensor (t = 0). The valve was operated for a 30% duty cycle and synchronized to the passing frequency (10.6Hz) of the simulated wakes. This corresponds to a dimensionless forcing frequency of F^+ = 0.34 (based on the distance from the VGJs to the blade trailing edge, SSLJ, and the mean passage velocity, U_{avg}). The average jet exit

velocity was adjusted with an inline pressure regulator. The peak unsteady blowing ratio ($B = U_{jet}/U_{local}$) was set at approximately 1.6 for the upstream jet row and 1.3 for the downstream row (due to physical limitations). The local freestream velocity was calculated from the local pressure coefficient at the respective VGJ site. VGJ actuation was always implemented on both blades simultaneously.

Data were acquired using a constant temperature hot film anemometer mounted to a 3-axis traverse above the cascade. The film is 50.8 μm in diameter, 1.02 mm long, and has a 200 kHz maximum frequency response. This device has a calibration uncertainty of ±0.08 m/s at a typical passage throughflow velocity of 5 m/s. The hotfilm signal was lo-pass filtered at 10kHz to reduce random electronic noise. A follower device is used to traverse the film along the blade surface at a specific wall distance (y/C_x). Data profiles were acquired at 57 streamwise locations, each ranging 2-5 mm apart. Measurements were concentrated in regions where separation was expected to occur. 14 data profiles were acquired at different y locations, ranging from 1.9-12.2 mm normal to the blade surface. The uncertainty in the distance from the wall was ±0.2 mm.

Data were processed to compute higher order turbulence statistics and intermittency following the same process outlined in Bons et al. [20]. At each follower position data were taken for 20 seconds (200,000 samples at 10 kHz). For the data in which the wake generator was used, data acquisition was phase locked to the rod exit sensor, each sensor pulse constituting one cycle. To process the data, all of the cycles were first averaged together to produce an ensemble-average mean velocity distribution. This average was subtracted from each cycle to eliminate the bulk unsteady motion of the flow from the statistical calculation. Then, each cycle was split into 24 equal time segments. Finally, the first segments of each cycle were all concatenated together and turbulence statistics were determined from the resulting set of data. Each of the subsequent 23 segments was concatenated together and analyzed in a similar fashion. The cycle period with the wake generator was approximately, T_{wake}=94 ms.

A Type KBC United Sensor Kiel probe was used to measure the total pressure loss (referenced to an upstream pitot probe) through the wake of the inner blade. The outer diameter of the sensing head is 3.175mm and the time constant is 15 seconds. The probe accurately measures total pressure within pitch and yaw ranges of ±45° with respect to the freestream flow direction. The sensing head of the probe was positioned at mid-span and traversed in a plane parallel to the cascade exit and 35 mm (24% C_x) downstream as illustrated in Fig. 2. The integrated wake loss coefficient is a measure of the changes in total pressure, and thus momentum, caused by viscous losses and mixing in the boundary layer. In this study the parameter is non-dimensionalized by the blade pitch to create an area-averaged loss parameter given by,

$$\gamma_{int} = \frac{1}{S} \int_{-S/2}^{S/2} \left(\frac{P_{T,in} - P_{T,ex}}{P_{T,in} - P_{S,in}} \right) ds \qquad (1)$$

Results

The results are presented in increasing levels of complexity; beginning with the baseline L1A performance, followed by the modified flow with unsteady wakes, and finally the application of VGJ flow control with unsteady wakes.

Baseline L1A (No Wakes, No VGJs):

Figure 3 shows both the predicted and measured c_p distribution for the L1A profile at three Reynolds numbers. The tailboards of the cascade were appropriately adjusted to yield approximately the same c_p distribution on the two blades (e.g. "inner" and "outer" – see Fig. 3 for a c_p comparison at Re=20,000). At Re = 20,000 and 40,000, the experimental data match the prediction quite well. The lower suction peak (4.2 as compared with the design value of 5.3) and the pressure plateau for $x/C_x > 0.6$ are characteristics of a massively separated blade profile. For the Re = 60,000 case, the c_p values are higher in the data compared to the prediction, though the suction peak is still at the same location (~0.6C_x). The maximum experimental c_p is just over 6, and the c_p values are slightly higher than the prediction for the entire forward portion of the blade ($x/C_x < 0.5$). The predicted separation bubble at $x/C_x = 0.75$ is not evident from the experimental data due to the lack of pressure taps in this region. However, a subsequent flow visualization study revealed a slight separation zone from about 70% - 75% C_x when the flow was viewed with injected smoke.
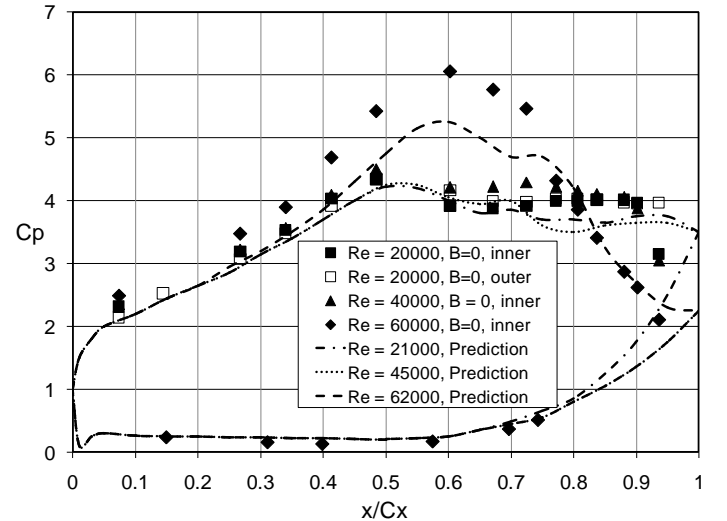

Figure 3: Measured and predicted c_p values for L1A profile at three Reynolds numbers.

The area-averaged wake total pressure loss data are compared to the corresponding prediction in Fig. 4. The losses rise dramatically for Re < 50,000, with the experimental and predicted values matching quite well for Re > 40,000.

18

Below Re = 40,000, the predicted loss levels out while the measurements show a steep rise to just under two times the predicted value at Re = 20,000. The underpredicted loss at very low Re is consistent with results from previous studies [7]. Likewise, the mismatch between peak c_p values in the prediction and experiment has been observed in similar studies using the AFRL design code. Design code improvements to address these inconsistencies are currently under investigation.
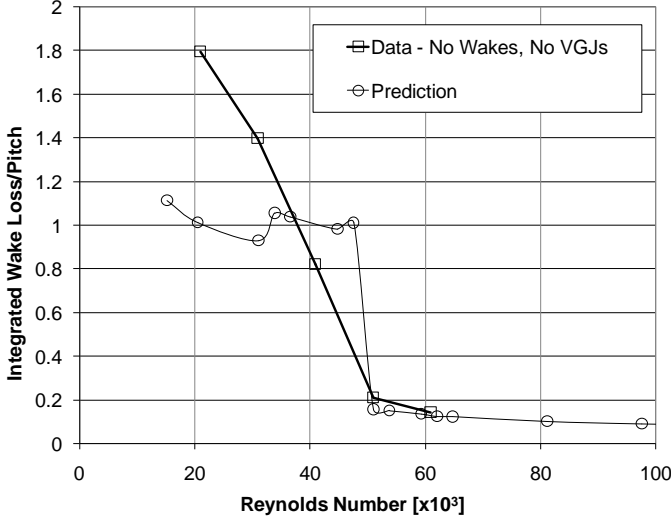

Figure 4: Prediction of area-averaged wake total pressure loss (γ_{int}) for L1A compared to experimental cascade measurements.

For the present study, it is serendipitous that the L1A cascade configuration exhibits a more aggressive loading that the predicted performance. For example, if the experimental blade was a turbine rotor, the elevated suction peak of the L1A cascade would yield an increase in the available work due to a larger integrated pressure force in the direction of rotation. Specifically, comparing the blade loading parameter, L:

$$L = \int_{blade} \left(\frac{P_{T,in} - P_{S,local}}{P_{T,in}} \right) \frac{\hat{e}_n \bullet \hat{e}_t}{C_x} ds \qquad (2)$$

The blade loading for the Re=60,000 experimental data in Fig. 3 is 18% larger than that calculated from the prediction at the same Reynolds number. The exaggerated magnitude of the wake total pressure loss at low Re (Fig. 4) also make the L1A cascade an ideal candidate for control, since there is significantly greater room for improvement.

Since the L1A blade design shares inlet and exit flow angles with the L1M and Pack B profiles, it is instructive to consider the effect of changes in loading on the boundary layer behavior at matched Re. Figure 5 includes contour plots of u_{mean}/U_{in}, u_{rms}/U_{in}, and skewness (of u) for all three blades at Re ≈ 20,000. The data are presented in wall normal vs. axial chord coordinates for compactness (see [13] for a more detailed description). The ordinate is the wall normal distance
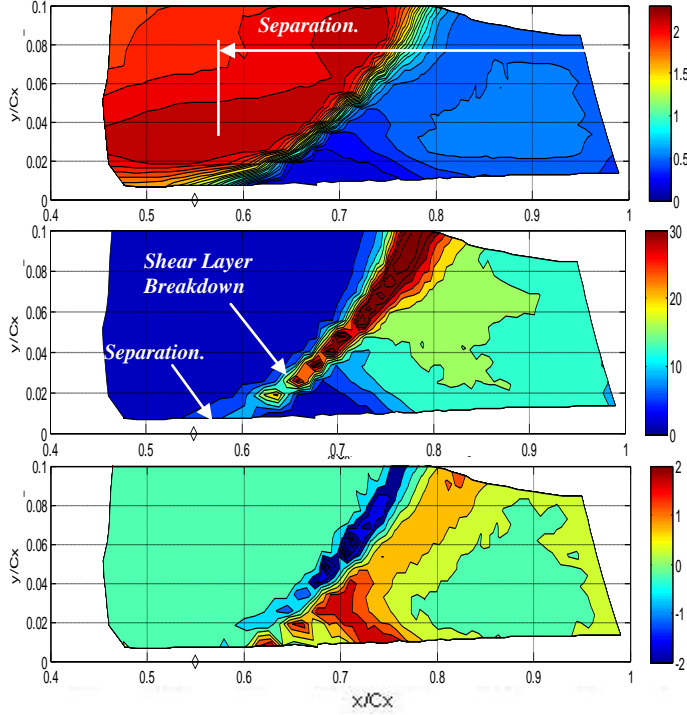
from the suction surface at the given axial chord location indicated on the abscissa. Locations of separation, shear layer transition, and reattachment (as appropriate) are noted on each

a) L1M

b) Pack B

19
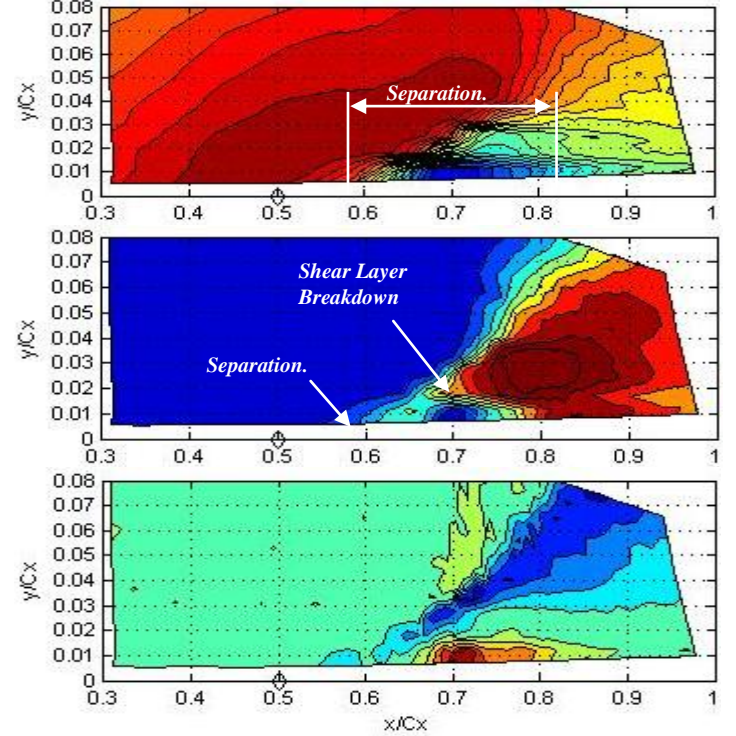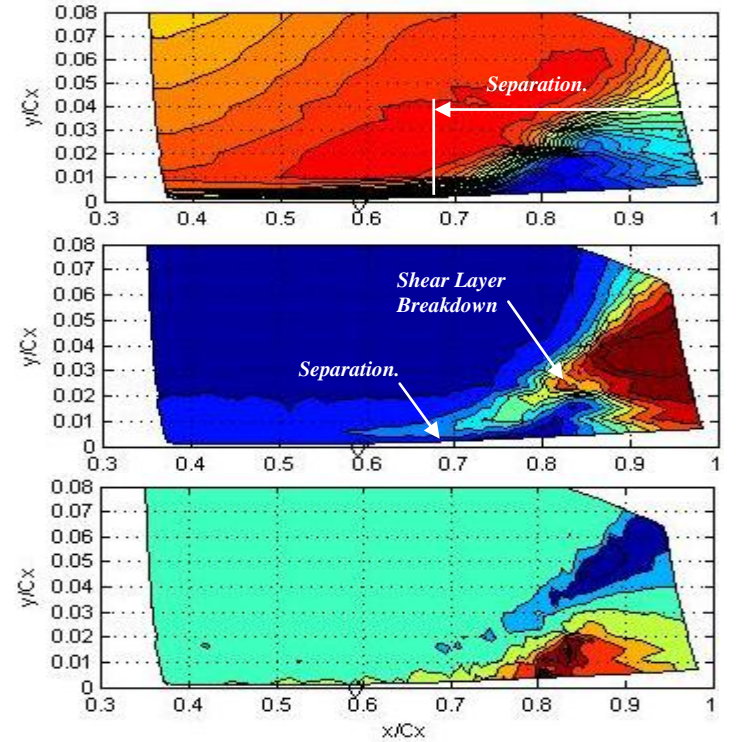
c) L1A

Figure 5: Time averaged contour plots of u_{mean}/U_{in} (top), u_{rms}/U_{in} [%] (middle) and skewness (bottom) presented in wall normal axial chord coordinates for a) L1M, b) Pack B, and c) L1A. All with no wakes and no VGJs at $Re_c=20,000$.

plot. In the absence of a wall shear measurement to precisely identify the separation location, it was determined from Fig. 5 that the separation locations were near 59%, 68%, and 57% C_x for the L1M, Pack B, and L1A blades respectively. This is identified in the plots by the region of rising near wall u_{rms} accompanied by a sharp drop-off in u_{mean} that occurs as the boundary layer becomes a separated free shear layer. Following separation, the region of rising turbulence lifts away from the wall and forms a separated free shear layer above a region of unsteady reverse near-wall fluid. After a short distance, this laminar shear layer begins to transition to a turbulent shear layer. As identified on the plots, the separated shear layer from the L1M begins turbulent breakdown near 70% C_x while breakdown occurs around 84% C_x for the Pack B and 64% C_x for the L1A. Based on these results, the laminar free shear layer extent is 11% C_x for the L1M (59% C_x separation to 70% C_x transition) and 16% C_x for the Pack B (68% C_x separation to 84% transition) and only 7% C_x for the L1A (57% C_x separation to 64% transition). The decreased transition length for the L1M and L1A blades is likely due to the more aggressive deceleration of the mean flow noted in the c_p profile. Figure 6 plots the acceleration parameter (K) on the suction surface for each of the 3 blades calculated using the predicted c_p distributions shown in Fig. 1.

$$K = \nu \frac{dU_e}{dx} \frac{1}{U_e^2} \qquad (3)$$

The design values of K shown in Fig. 6 clearly show that the L1A profile presents a more aggressive diffusion (K<0) to the passage flow. Using a spline fit to the Re=60,000 experimental c_p data in Fig. 3, the acceleration parameter was estimated for the present L1A cascade as well. This is shown with the predicted data in Fig. 6 and displays the heightened diffusion (K < 0 for $x/C_x > 0.6$) experienced by the flow in the cascade relative to the periodic calculation. Given that adverse pressure gradients are known to be destabilizing, the earlier separation and breakdown of the L1A separated shear layer, as compared to the L1M and Pack B, are to be expected.
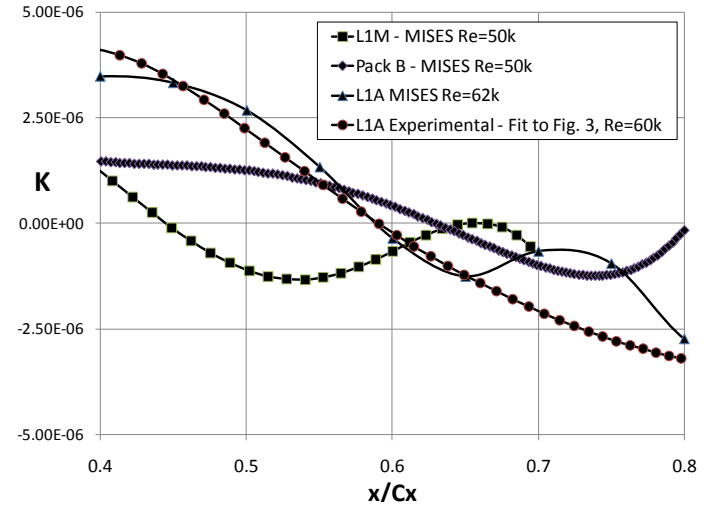

Figure 6: Suction surface acceleration parameter plotted against x/C_x calculated from c_p predictions for the L1A, Pack B, and L1M profiles shown in Fig. 1 and for the L1A experimental data in Fig. 3 (Re=60k).

For the L1M and Pack B blades, the turbulent breakdown of the shear layer spreads rapidly down to the wall. The peak level of turbulence in the turbulent shear layer reaches down to the nearest wall measurement location by 82% C_x for the L1M profile, as indicated in Fig. 5, while the maximum turbulence level never quite penetrates down to the blade surface for the Pack B. It is thus concluded that the separated region successfully reattaches for the L1M around 82% C_x while the Pack B separation does not fully reattach in the measurement domain. By comparison, the L1A separation is complete and total. Evidently, the free shear layer breakdown occurs in a region of the blade with such strong curvature (Fig. 6) that the heightened mixing never manages to propagate down through the separation bubble to reattach the flow. The entire aft portion of the blade is characterized by unsteady flow recirculation. This explains the excessive wake loss values at low Reynolds numbers shown in Fig. 4.

Regions of unsteady reverse flow can be detected as areas of positive skewness in the near wall region of Fig.5. Because

20

the hot-film is only sensitive to velocity magnitude, any negative (reverse flow) velocities are positively justified resulting in positive skewness values in regions of low or near-zero u_{mean}. All three blades show regions of strong positive skewness beneath the separated free shear layer. The streamwise extent of this unsteady reverse-flow region is about 70% longer in the Pack B and L1A cases compared to the L1M. Because the flow turning is not yet complete at this blade location, the extended streamwise bubble length causes the Pack B and L1A free shear layers to migrate further from the blade surface before breakdown. Following the trajectory of the separating free shear layer and continuing out into the freestream are bands of strongly negative skewness as seen in Fig. 5. These regions are indicative of high velocity flow punctuated by short bursts from lower momentum pockets. Thus, Cattanei et al. used skewness as a method of identifying flow transition [21]. As expected, these transition indicators suggest the location of transition occurs in the region of the shear layer breakdown as mentioned above and indicated in the plots. This conclusion is supported by intermittency contour plots in the same vicinity (not shown).
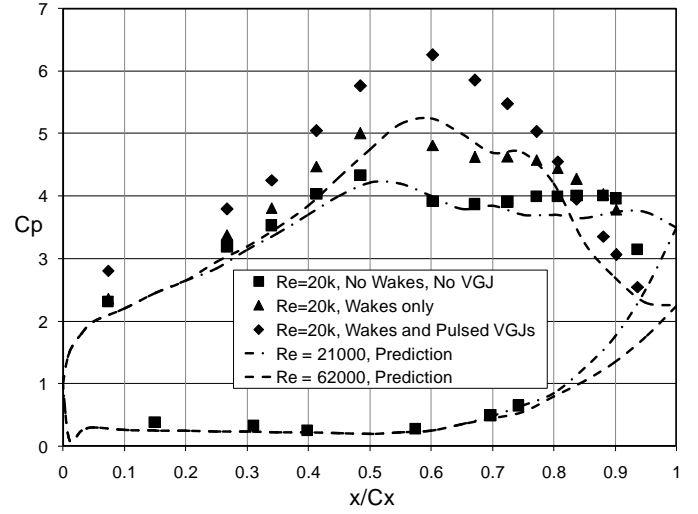

Figure 7: c_p data for baseline, wakes, and wakes + upstream VGJ cases at Re=20,000 compared to prediction for L1A.

L1A with Unsteady Wakes (No VGJs):

When the wakes are introduced into the inlet plane of the cascade, the time-averaged c_p distribution shows an immediate benefit (Fig. 7). The peak c_p approaches 5 and the time-averaged separation is reduced considerably. This is also evident in a reduced wake loss (γ_{int}) of 0.8 (less than half of the baseline value at Re = 20,000 in Fig. 4). Figure 8 shows phase-locked u_{mean}/U_{in} and u_{rms}/U_{in} data for 12 discrete phases through the wake passing period in the same format as Fig. 5. Evidence of the wake is observed first in the u_{mean} plot at t/T = 0.77 with a local acceleration convecting above the separated shear layer at $x/C_x = 0.75$ and $y/C_x = 0.06$. This acceleration is due to the accelerated flow over the leading side of the
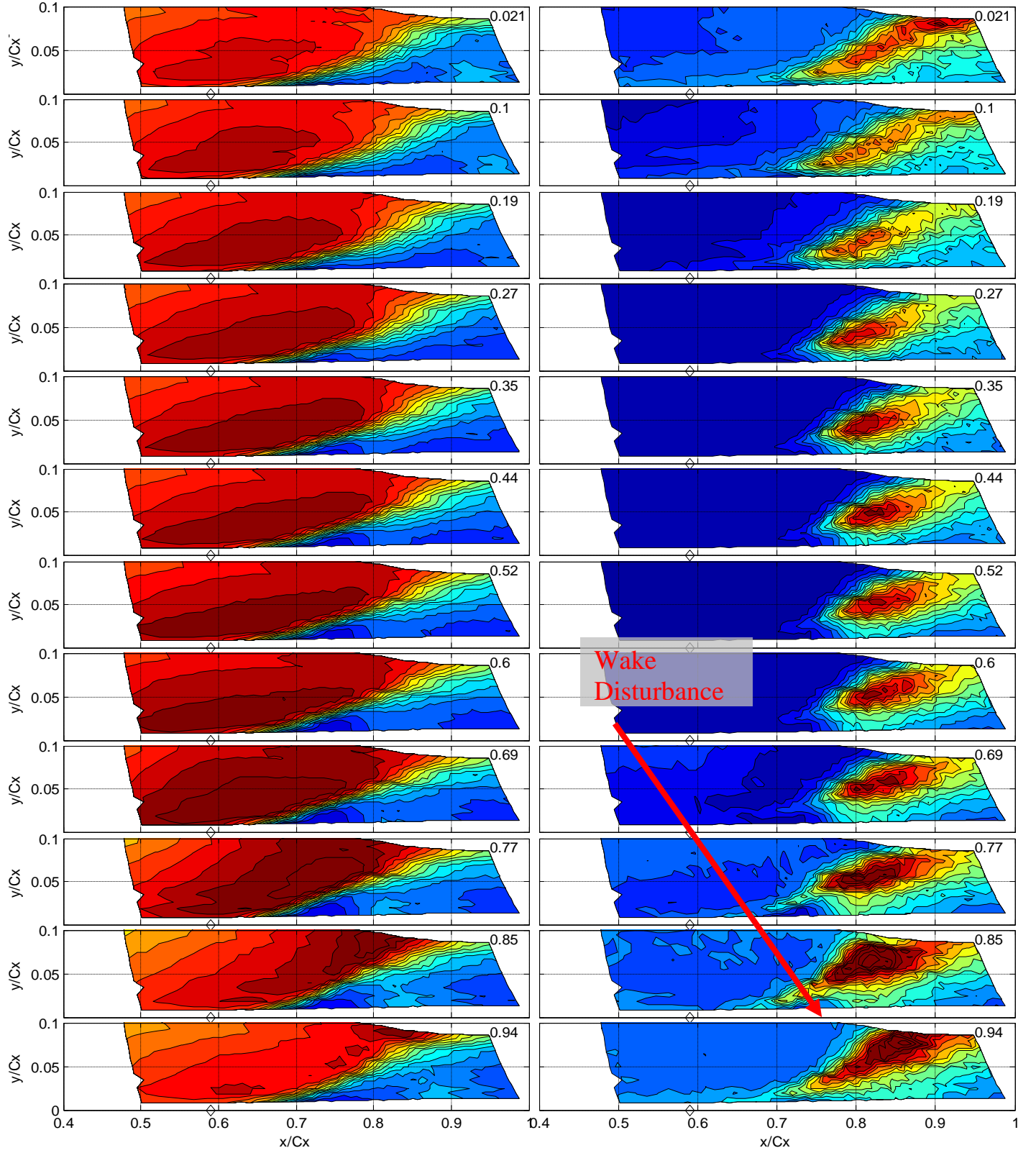
a) u_{mean}/U_{in}

a) u_{mean}/U_{in}

b) u_{rms}/U_{in}

Figure 8: Contour plots of u_{mean}/U_{in} and u_{rms}/U_{in} at 12 discrete phases of wake passing period on the L1A profile. Data for wakes only (no VGJs). Re = 20,000. Colorbars identical to Fig. 5.
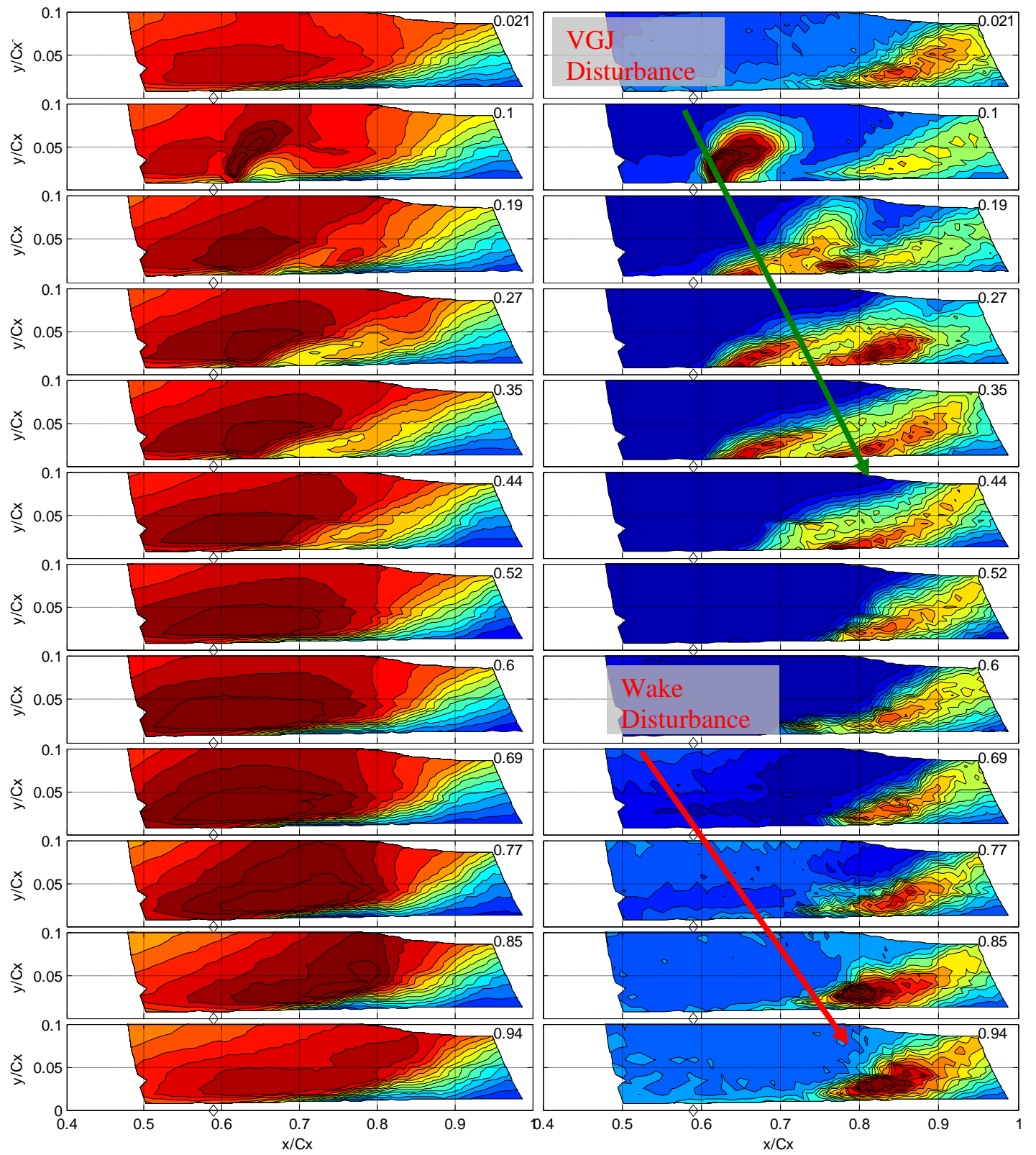
a) u_{mean}/U_{in}

b) u_{rms}/U_{in}

Figure 9: Contour plots of u_{mean}/U_{in} and u_{rms}/U_{in} at 12 discrete phases of wake passing period. Data for wakes with upstream VGJs at 59%C_x with B=1.6. Re=20,000. Colorbars identical to Fig. 5.

traversing bar and has been noted before [22]. The acceleration is followed immediately by the bar wake, with lower velocity and elevated u_{rms} (5% as compared with <1%). The separated shear layer is gradually destabilized by the elevated turbulence and a tongue of elevated u_{rms} projects upstream from $(x/C_x=0.75, y/C_x=0.04)$ to $(x/C_x=0.7, y/C_x=0.02)$ between $t/T = 0.77$ and 0.94. Peak turbulence levels in the separated shear layer reach a maximum of 24% during this period, which convects along the separated shear layer from $(x/C_x=0.8, y/C_x=0.05)$ at $t/T = 0.77$ to $(x/C_x=0.88, y/C_x=0.08)$ at $t/T = 0.94$.

For the Pack B blade profile, Reimann et al. [22] noted the same phenomena during the wake passing. In that case, the elevated turbulence and earlier shear layer breakdown caused by the wake disturbance resulted in a reorientation of the entire separated shear layer down closer to the blade. The region of near wall low-momentum fluid ($u_{mean}/U_{in} < 0.7$), was thinned considerably by this motion resulting in temporary reattachment followed by a protracted "calmed zone" [10,21,24,25] of low turbulence boundary layer behavior before returning to separation. The more highly loaded L1A response is markedly different in this regard. While the wake does alter the shear layer breakdown and temporarily amplify the instabilities in this region, the heightened mixing does not reattach the boundary layer. A very localized increase in u_{mean} is evident at $x/C_x=0.82, y/C_x=0.02$ due to the elevated turbulence, but this region quickly loses continuity with the shear layer and convects downstream alone. Once the wake has completely passed, a very slight "calming effect" is evident in depressed u_{rms} levels from $t/T = 0.1 - 0.19$. At this time, the u_{rms} levels recover their pre-wake levels and remain there until the next wake passing. Comparing the Pack B and L1A results, the proximity of the separated shear layer to the wall appears to play a role in determining if the wake disturbance field causes a reattachment (Pack B) or not (L1A). When the separated shear layer is too far removed from the blade surface, the wake-induced unsteadiness is not able to penetrate down to the wall and fails to effectively reenergize the near wall (separated) fluid.
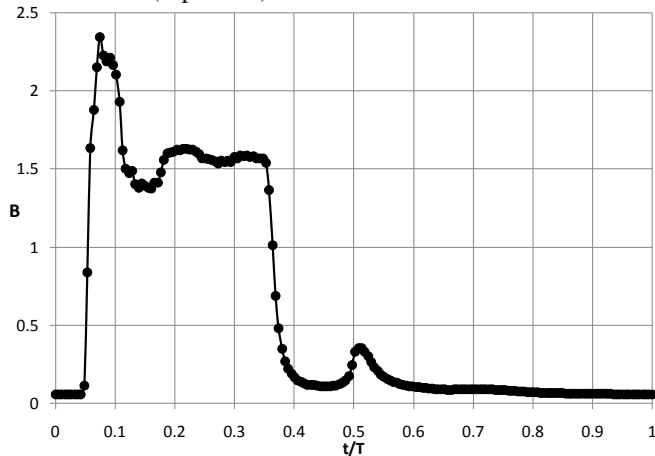

Figure 10: Pulsed VGJ blowing ratio plotted against dimensionless time. x/C$_x$ = 59%

L1A with Unsteady Wakes and VGJs:

Figure 9 has the same format as Fig. 8, but includes the effect of pulsed VGJs at $x/C_x = 0.59$. As before, the wake effect is evident from $0.77 < t/T < 0.94$, followed by the jet effect beginning at $t/T = 0.1$. The jet is injected downward into the measurement plane which is located 4d below the injection point. Thus, the first evidence of the jet is at $x/C_x = 0.61$. The jet remains "on" until $t/T = 0.35$. The jet signature in the u_{rms} plots changes significantly over the pulse duration due to non-ideal feed plenum dynamics. Figure 10 shows the pulse exit velocity taken with a hotfilm located at the hole exit and no freestream flow (t=0 is from the wake generator rod sensor). Though the average exit blowing ratio is B≈1.6, there is a significant overshoot up to B = 2.3. The effect of this overshoot is particularly evident when the velocity data are viewed in a time-space format. Figure 11 shows side-by-side time-space plots of u_{rms} for the wakes only and wakes + VGJ cases at $y/C_x = 0.013$ & 0.038. (Note: The yellow highlighted band indicates the separated shear layer location for the baseline case with no wakes and no VGJs.) The full pulse event is evident at $y/C_x = 0.013$ while only the pulse overshoot penetrates out to $y/C_x = 0.038$ at $x/C_x = 0.61$. The data at both y locations show a reduction in u_{rms} levels directly following the jet disturbance, with a gradual increase before the wake event appears. Perhaps the most noteworthy effect of the jet is the adjustment in the mean position of the free shear layer. At $y/C_x = 0.038$, the line of peak u_{rms} with wakes always remains between $0.76 < x/C_x < 0.84$. With flow control, this mean position moves downstream to $0.85 < x/C_x < 0.90$. This thinning of the separation zone is likewise evident in a sharply reduced wake loss ($\gamma_{int} = 0.31$) and a fully recovered time-average c_p distribution (Fig. 7). In fact, both the γ_{int} and the c_p are very near the fully-attached, high Re values (Re=60,000) shown in Figs. 3 and 4. Thus, the pulsed VGJ flow control at $x/C_x = 59\%$ (just after the uncontrolled separation location and the peak c_p) corrects the separation to a greater extent than do wakes alone.

For the Pack B, Bloxham et al. [10] reported that the separation bubble size was minimized for an optimum synchronization of VGJs and wakes with the jet being activated precisely between consecutive wakes (just before the relaxation of the calmed zone). The synchronized VGJ + wake performance was notably better than that achieved with either wakes or VGJs alone. A similar synchronization was performed with the L1A configuration wherein the relative timing of the two events was varied in $t/T = 0.05$ increments. Figure 12 shows the wake loss measurements normalized by the wake loss value with wakes only. (Thus, a value of unity indicates no effect of flow control.) For the upstream VGJ location, the data show no significant optimum with regard to synchronization. In fact, the integrated wake loss was approximately the same whether VGJs were employed with or without unsteady wakes. Similar results were achieved using steady VGJ blowing (B = 1.4) at $x/C_x = 59\%$, with and without unsteady wakes.
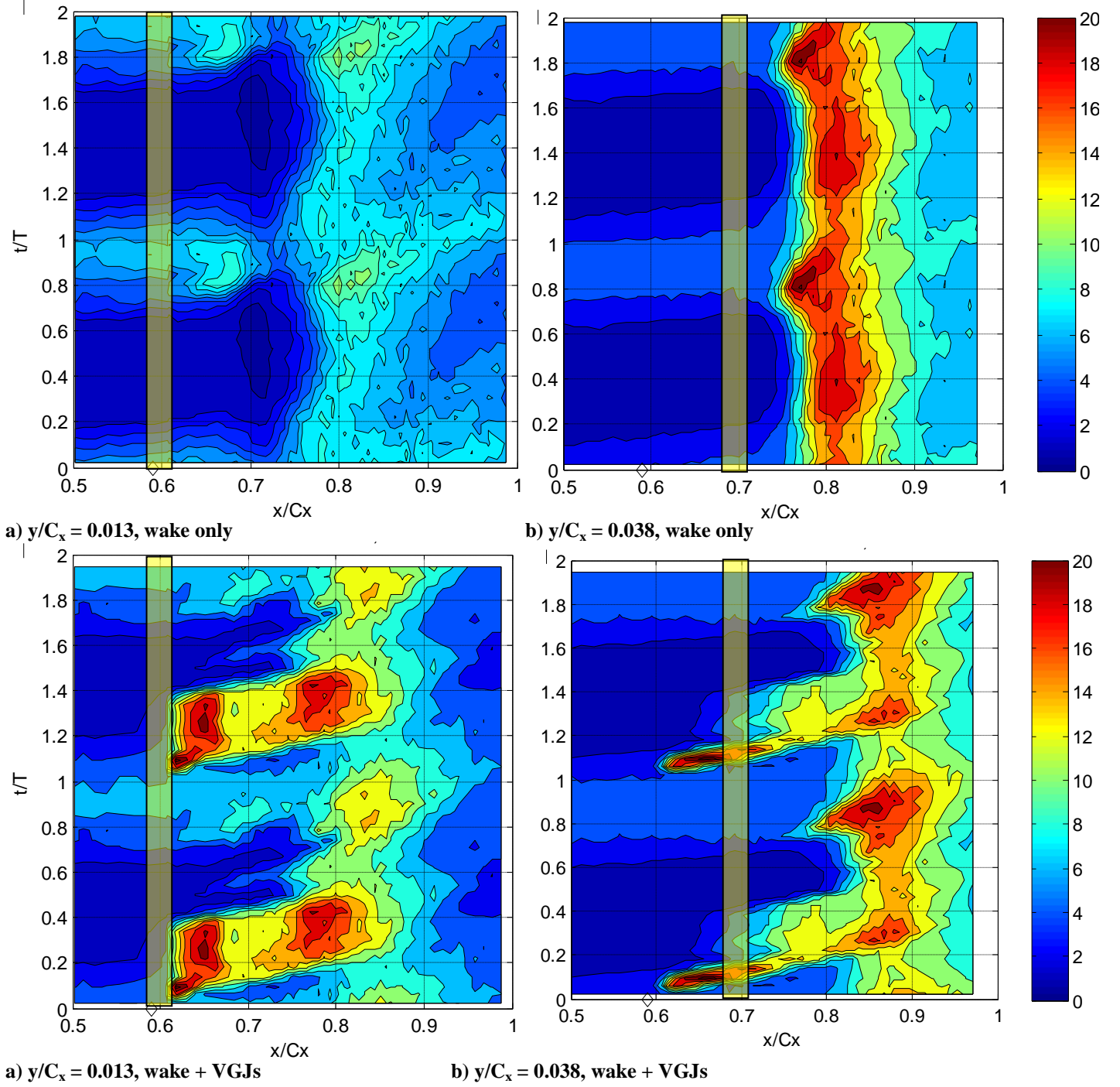
a) y/Cx = 0.013, wake only

b) y/Cx = 0.038, wake only

a) y/Cx = 0.013, wake + VGJs

b) y/Cx = 0.038, wake + VGJs

Figure 11: Time space plots of u_{rms}/U_{in} at y/C_x = 0.013 & 0.038 for wakes only and wakes + VGJs. Yellow highlighted band indicates separated shear layer location for baseline case (no wakes, no VGJs). Re=20,000

On the other hand, actuation at the downstream VGJ location (72%C_x) does show a significant effect of synchronization. The loss minimum in Fig. 12 occurs for 0.1 < t/T < 0.2. Looking at the unsteady shear layer location shown in Fig. 8, it is apparent that this downstream actuation location is well into the separation zone. Thus it is significant

that control is still effective deep into the separation bubble. Due to physical limitations of the facility, the blowing ratio used in this study was 1.3. It is anticipated that a higher blowing ratio pulse may be as effective as the upstream location for B = 1.6, with the added benefit of a synergy due to synchronization. Thus the downstream location may actually

25

be the optimum site for flow control though it is well past the blade suction peak. The phase-locked data taken with upstream VGJ actuation (Figs. 8,9, & 11) were acquired with a phase of t/T = 0.05. This was selected based on the fluid particle transit time between 59% and 72% Cx (approximately t/T = 0.1). Thus, the optimal phasing in Fig. 12 corresponds to approximately the same timing between wakes and VGJs (i.e. the jet actuates between wake disturbances similar to the findings of Bloxham et al. [10]). It is worth noting that in the absence of unsteady wakes, pulsed VGJ actuation at 72% C_x has a very minimal benefit on the wake losses ($\gamma_{int} \cong 1.4$). This contrasts sharply with the result from the upstream location where VGJs are as effective with or without wakes. Apparently, the separated shear layer is too far removed from the wall to be influenced significantly at the 72%C_x location.
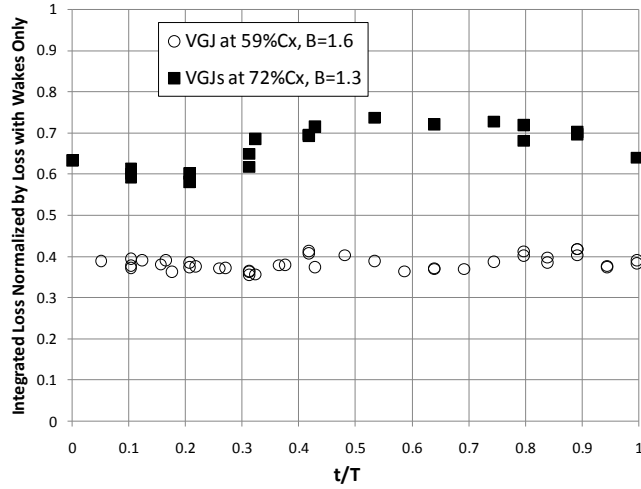

Figure 12: Wake total pressure loss normalized by loss with wakes only. Data for VGJ actuation at 59%C_x with B = 1.6 and 72%C_x with B = 1.3. plotted against dimensionless time. Re = 20,000

Perhaps the most telling result from this application of flow control (apart from the c_p and γ_{int} data) is the time-averaged location of the separated shear layer (Fig. 13). This figure shows contour plots of time-averaged u_{mean}/U_{in} for the baseline, wake only, upstream VGJ only, and wake + upstream VGJ cases. Since the jets create a near-wall disturbance, they are most effective at bringing the time-averaged shear layer down to the wall. The wake is a global disturbance, and has a uniform effect over the entire shear layer (both near-wall and far-field). The combination of wakes + upstream VGJs produces a diffusion on the aft portion of the blade that is very near design (Figs. 7 and 3). As noted from the time-space plots (Fig. 11), the addition of jets to the unsteady wake flowfield has the effect of moving the mean location of the shear layer downstream (from 0.76 < x/C_x < 0.84 to 0.85 < x/C_x < 0.90 for y/C_x = 0.038). Remarkably, this downstream position becomes a new equilibrium location for the separation. During the period between pulses, the shear layer does not migrate upstream to the wake-only mean location or to the baseline location (0.67

< x/C_x < 0.70 for y/C_x = 0.038 as indicated on Fig. 11). This phase lag in the recovery of the separated boundary layer is similar to results reported by Bons et al. [25] for the Pack B.

a) **Baseline, no wakes, no VGJs**

b) **Wakes only**

c) **Upstream VGJs only**
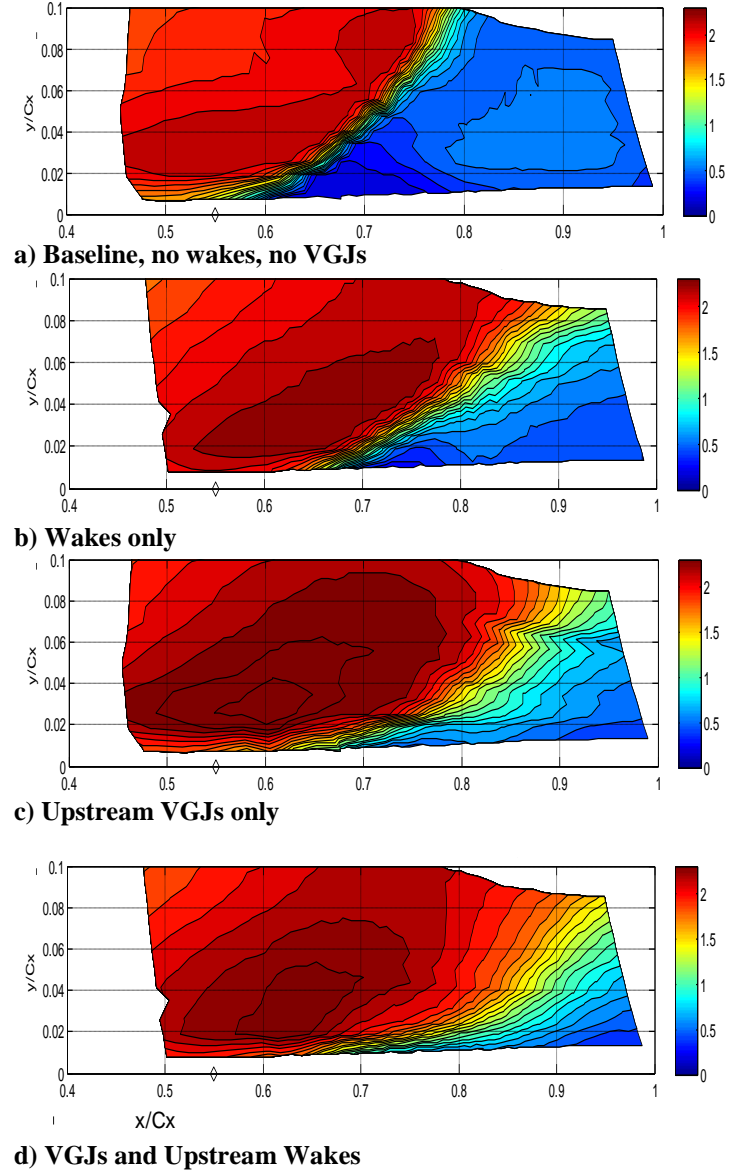
d) **VGJs and Upstream Wakes**
Figure 13: Contour plots of time-averaged u_{mean}/U_{in}. Data for baseline, wakes only, upstream VGJs only, and wakes with upstream VGJs. Re=20,000

Following a pulsed jet disturbance, the boundary layer was found to remain in a controlled state for 8-10 convective timescales after the jet was terminated (convective timescale = SSLJ/U_{avg}). The convective timescale for the present application is approximately 0.03 seconds, or one third of the forcing period. Thus, the forcing frequency is too high to allow recovery of the fully separated flow condition. The blade is essentially operating at a new quasi-stable equilibrium condition, with significantly reduced separation. To validate this conclusion, the wake generator was temporarily modified

by eliminating alternate rods; thus decreasing the F^+ to 0.17. With this modification, the integrated wake loss jumped by roughly 50% for both the wake-only and wake + upstream VGJ cases. Thus, the wake frequency range relevant to LPTs ($F^+ \sim 0.3$) is sufficient to capitalize on the phase-lagged boundary layer response to disturbances.

Nomenclature

B	jet blowing ratio ($U_{jet}/U_{e,59\%Cx}$)
C_x	blade axial chord (0.143m)
c_p	pressure coefficient ($(P_{T,in}-P_S)/(P_{T,in}-P_{S,in})$)
F^+	non-dimensional forcing frequency ($f/(U_{avg}/SSLJ)$)
K	acceleration parameter (Eq. 3)
L	distance between rods
L	blade loading parameter (Eq. 2)
P	pressure
Re_c	axial chord Reynolds number ($\rho U_{in}C_x/\mu$)
S	blade spacing
SSLJ	suction side length from jet location to trailing edge
T	rod passing period (94 ms)
U	velocity magnitude
Zw	Zweifel loading coefficient
d	jet hole diameter (2.6mm)
ê	unit vector
f	forcing frequency
t	time (s)
u_{mean}	mean streamwise velocity
u_{rms}	fluctuating streamwise velocity
x	streamwise coordinate
y	blade normal coordinate
z	spanwise coordinate
γ_{int}	integrated wake pressure loss coefficient (Eq. 1)
ν	kinematic viscosity
μ	dynamic viscosity
ρ	density
φ	flow coefficient ($U_{in,axial}/U_{rod}$)

subscripts

S	static
T	total
avg	average from jet location to trailing edge
axial	axial direction
c	axial chord
e	local boundary layer edge
ex	cascade exit conditions
in	cascade inlet conditions
jet	VGJ conditions
mean	mean
n	surface normal direction
rms	root mean square
rod	wake generator rod
t	surface tangent direction
59%Cx	jet injection location

References

[1] Lake, J., King, P., and Rivir, R., "Reduction of Separation Losses on a Turbine Blade with Low Reynolds Number", AIAA paper #99-0242, 1999.

[2] Rivir, R.B., Sondergaard, R., Bons, J.P., and Lake, J.P., 2000, "Passive and Active Control of Separation in Gas Turbines", presented at AIAA Fluids 2000 in Denver CO, 19-22 June, 2000, AIAA paper #2000-2235.

[3] Volino, R.J., "Passive Flow Control on Low-Pressure Turbine Airfoils," *Proceedings of ASME Turbo Expo 2003: Power for Land, Sea, and Air*, GT2003-38728.

[4] Torre, D., Vazquez, R., de la Rosa Blanco, E., and Hodson, H.P., 2006, "A New Alternative for Reduction of Secondary Flows in Low Pressure Turbines," presented at IGTI 2006 in Barcelona, Spain, paper #GT2006-91002.

[5] Huang, J., Corke, T.C., and Thomas, F.O., 2003, "Plasma Actuators for Separation Control of Low Pressure Turbine Blades," AIAA #2003-1027.

[6] Volino, R. J., "Separation Control on Low-Pressure Turbine Airfoils Using Synthetic Vortex Generator Jets," *Proceedings of ASME Turbo Expo 2003: Power for Land, Sea, and Air*, GT2003-38729.

[7] Sondergaard, R., Bons, J. P., and Rivir, R. B., 2002, "Control of Low-Pressure Turbine Separation Using Vortex Generator Jets," *AIAA J. Propulsion and Power*, Vol. 18, No. 4, pp. 889-895. Jul/Aug 2002.

[8] McQuilling, M. and Jacob, J., 2004, "Effect of Chord Location on Separation Control with Vortex Generator Jets on Low Pressure Turbine Blades," presented at the 2nd AIAA Flow Control Conference in Portland, OR, 28 June – 1 July (paper #AIAA 2004-2205).

[9] D.H. Olson, D. Reimann, M. Bloxham, and J.P. Bons, "The Effect of Elevated Freestream Turbulence on Separation Control with Vortex-Generating Jets," presented at the AIAA 43rd Aerospace Sciences Meeting and Exhibit in Reno, NV, 10-13 Jan 2005 (paper #AIAA 2005-1114).

[10] M. Bloxham, D. Reimann, K. Crapo, J. Pluim, and J.P. Bons, "Synchronizing Separation Flow Control with Unsteady Wakes in a Low-Pressure Turbine Cascade," presented at the 2007 IGTI conference in Montreal, 14-17 May 2007. Paper #GT2007-27529

[11] Sondergaard, R., Bons, J.P., and Rivir, R.B., 2002, "Reducing Low-Pressure Turbine Stage Blade Count Using Vortex Generator Jet Separation Control," presented at the 2002 International Gas Turbine Institute (IGTI) Conference in Amsterdam, The Netherlands, (paper #GT-2002-30602).

[12] J.P. Bons, L.C. Hansen, J.P. Clark, P.J. Koch, and R. Sondergaard, "Designing Low-Pressure Turbine Blades with Integrated Flow Control," presented at IGTI 2005 in Reno, NV, June 2005. Paper # GT2005-68962.

[13] D. Reimann, M. Bloxham, K.L. Crapo, J.D. Pluim, and J.P. Bons, "Influence of Vortex Generator Jet-Induced Transition on Separating Low Pressure Turbine Boundary Layers," presented at the 3rd AIAA Flow Control Conference in San Francisco, 5-8 June, 2006 (paper #AIAA 2006-2852)

[14] Praisner, T. J., Grover, E. A., Rice, M. J., and Clark, J. P., 2004, "Predicting Transition in Turbomachinery, Part 2- Model Validation and Benchmarking," ASME Paper No. GT-2004-54109.

[15] McQuilling et al., submitted to AIAA ASM Meeting, Jan 2008.

[16] Clark, J. P., and Grover, E. A., 2007, "Assessing Convergence in Predictions of Periodic-Unsteady Flowfields," ASME *Journal of Turbomachinery*, Vol. 129, No. 4, pp. 740-749.

[17] Huber, F., 2004, Personal Communication to J. P. Clark.

[18] Dorney, D. J. and Davis, R. L., 1992, "Navier-Stokes Analysis of Turbine Blade Heat Transfer and Performance," *Journal of Turbomachinery*, Vol. 114, pp. 795-806.

[19] Praisner, T. J. and Clark, J. P., 2007, "Predicting Transition in Turbomachinery, Part 1- A Review and New Model Development," *Journal of Turbomachinery*, Vol. 129, pp. 1-13.

[20] Bons, J.P., Bloxham, M. and Reimann, D., 2006, "Separated Flow Transition on an LP Turbine Blade with Pulsed Flow Control," presented at the 2006 IGTI conference in Barcelona, 8-11 May, 2006. Paper #GT2006-90754.

[21] Cattanei, A., Zunino, P., Schroder, T., Stoffel, B., and Matyschok, B., 2006, "Detailed Analysis of Experimental Investigations on Boundary Layer Transition in Wake Disturbed Flow," presented at the 2006 IGTI conference in Barcelona, 8-11 May, 2006. Paper #GT2006-90128.

[22] D. Reimann, M. Bloxham, J. Pluim, and J.P. Bons, "Comparison of Spanwise Wake and Discrete Jet Disturbances on a Separating Low-Pressure Turbine Blade," presented at the AIAA 45th Aerospace Sciences Meeting and Exhibit in Reno, NV, 8-11 Jan 2007 (paper #AIAA 2007-0525).

[23] Gostelow, J.P., and Thomas, R.L., 2003, "Response of a Laminar Separation Bubble to an Impinging Wake," *Proceedings of ASME Turbo Expo 2003: Power for Land, Sea, and Air*, GT2003-38972.

[24] Stieger, R.D., and Hodson, H.P., 2003, "The Transition Mechanism of Highly-Loaded LP Turbine Blades," *Proceedings of ASME Turbo Expo 2003: Power for Land, Sea, and Air*, GT2003-38304.

[25] Bons, J. P., Sondergaard, R., and Rivir, R. B., "The Fluid Dynamics of LPT Blade Separation Control Using Pulsed Jets," *ASME Journal of Turbomachinery*, Vol. 124, Jan. 2002, pp. 77-85.

28